Technische
Universität
München

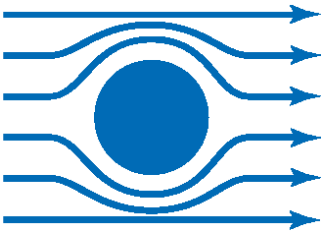

Walther-Meißner
Institut

Indian Institute
of Technology
Madras

Investigation of the amplitude of the spin Hall magnetoresistance in antiferromagnetic FeO

Master's thesis

Mayank Sharma
(PH19M005)

Supervisor

Prof. Dr. Rudolf Gross and Prof. Dr. MS Ramachandra Rao

Advisor

Dr. Matthias Opel

Garching – 18. Juni 2021

Contents

1 Introduction

In 1973, when Dr. Martin Cooper (general manager at Motorola communications) used a device weighing 1.1 kg to make the first public mobile phone call, nobody thought the device would weigh few hundred grams in future. What is even more interesting is the main purpose for which the device was created would become secondary, whereas collection and storage of data would become its primary job. Today, when half of the world's population have their individual smartphone and they are constantly capturing multimedia, data storage have become inseparable part of our everyday lives. In order to store this enormous amount of digital data we need physical devices, which have led to the creation of large data storage centres across the globe. These data centres consume a big percentage of global power and with the current technology the data centres are predicted to consume 20% of the global power by 2025. This creates a demand for further miniaturization of the microelectronic components and with that comes the evergrowing demand for low-powered data storage and processing.

With this high demand of data storage, the general approach of encoding a message have not changed much, as information is usually carried by the charge of electrons. However, beside their charge, electrons also exhibit an additional degree of freedom: *spin*. It has gained much interest in recent years giving rise to the research field of *spintronics*, which aims towards the implementation of current technology via spintronics devices [1, 2]. Spintronics in general terms involves the different concept of transfer and storage of information by manipulation of the intrinsic spin and its associated magnetic moment, in addition to the charge of the electron.

The initial idea of magnetic recording was proposed by O. Smith in 1888 [3] which was followed by first magnetic tape recorders in 1930s. The technology evolved by great extent in the meantime, the basic concept of using magnetic state as logical bit which can be read out afterwards is still analogous today. The commonly used strategy for the read-out of magnetic states is to employ magnetoresistive effects i.e. to use the materials electrical resistivity dependence of the magnetization orientation. In late 1980s came the big breakthrough of giant magnetoresistance (GMR) by Albert Fert [4] and Peter Grünberg [5] which revolutionised the data storage technology and led the duo winning the 2007 Nobel Prize in Physics. The GMR effect has its own limitations. It requires a tri-layer system of a ferromagnet a non-magnetic layer and a ferromagnet just to make the read head which requires additional power and movement over each bit to read the data. In 2013, another fundamentally different magnetoresistive effect was reported by Nakayama, Althammer and co-workers [6–8] called spin Hall magnetoresistance (SMR) in normal metal (NM)/ferrimagnetic insulator (FMI) bilayers. SMR is mediated by the spin current flow across the NM|FMI interface, producing a resistivity change in the NM depending on the magnetisation orientation of the ferrimagnetic insulator.

In the past decade the normal metal and ferromagnetic material hybrid structures have been presented as well established basic elements in the field of data storage. For next generation of data storage technologies using spintronics, antiferromagnetic (AF) materials have become the focus of interest [9–18]. Since, the net magnetisation in antiferromagnets is compensated by the antiparallel alignment of the neighbouring magnetic moments, they

do not exhibit magnetic stray fields. Eliminating the possibility of disruptive cross talk in between adjacent bits and hence allow for higher data storage density devices. Furthermore they promise to increase the dynamics [19] and the lack of net magnetisation makes them robust against the external magnetic fields [18,20,21] preventing memory loss due to accidental switching. In recent past AF insulators have been studied extensively and phenomena like the spin Hall effect [22–25], the spin-Nernst and spin-Seebeck effects [16,26–29] and other spin transport phenomena [30–36] were observed. The advantageous property of net zero macroscopic magnetisation in AF, presents a challenge when it comes to the read-out of the stored states and to use them in data storage, a robust detection scheme is required.

The SMR effect originates from the interaction of spin and charge currents between a non-magnetic metal, exhibiting spin Hall effect (SHE) [37] with finite spin polarization **s** at the interface and a magnetic insulator with magnetisation **M**. This interaction between **M** and **s** results in exchange of spin-angular-momentum and is physically observed as characteristic dependence of resistivity on angle between the two (**M**, **s**) [8]. From its first observation in Pt | $Y_3Fe_5O_{12}$(YIG) heterostructures [6] and theoretical explanation by a non equilibrium proximity effect [8], the SMR model has been confirmed multiple times in Pt | YIG [6, 7, 38–42]. The effect was further studied in normal metal | collinear ferromagnetic insulator systems like Pt | Fe_3O_4 [7], Ta | YIG [39], Pt | $CoFe_2O_4$ and Pt | $NiFe_2O_4$ [43]. More recently the SMR effect sensitivity to the sublattice magnetisation in antiferromagnets [44–48] has been confirmed, making it a viable and sensitive probe to read the stored information. In addition to the sensitivity it is simple to implement, it only requires a planar Hall bar electrode in a bilayer thin film system.

The SMR manifests itself in characteristic oscillations of the resistivity and the phase is already well understood. The phase is shifted by $90°$ in case of antiferromagnets relative to ferrimagnets. The amplitude is still under debate, for instance hematite ($\alpha-Fe_2O_3$) has a much larger amplitude than YIG. The amplitude is governed by real part of spin mixing interface conductance $g_r^{\uparrow\downarrow}$ and parameters on which this factor depends is still not very clear. In order to get further insight into this, we study different iron based magnetically ordered oxides.

This thesis is organized as follows: in Chap. 2, we provide an overview of the theoretical concepts essential for this work. An introduction to different iron oxides, experimental details and different measurement techniques used in this work are discussed in the Chap. 3. In the Chap. 4, we discuss the growth of FeO films on sapphire and MgO substrates and later in the chapter we present the SMR measurements performed using the angle dependent magnetoresistance (ADMR). The thesis is concluded with summary and an outlook in Chap. 5.

2 Theory Overview

In order to understand devices harnessing the spin degree of freedom, it is essential to familiarize oneself with the concept of spin currents as well as with the methods enabling their generation and detection. Therefore, in this chapter we give a brief overview of electronic spin currents (Sec. 2.1) and the spin Hall effect (SHE, Sec. 2.2), representing the most prominent way for generating (direct SHE) and detecting (inverse SHE) pure spin currents. Later, we discuss the spin Hall magnetoresistance (SMR, Sec. 2.3) effect, which offers a practical way to characterize the SHE physics of a normal metal (NM) when combined in bilayer structures with a magnetically ordered insulator (MOI) that have been multiply highlighted in literature [6,7,38–44,49–52]

2.1 Spin Currents

Our intuitive understanding of charge currents naturally develops the picture of moving electrons along a certain direction. However, in addition to being the carriers of elementary charge $q_e = -e$ (with $e > 0$), electrons also possess a second degree of freedom: an intrinsic spin angular momentum $S = \pm\frac{\hbar}{2}$. This intrinsic property has quantum-mechanical origin that measuring spin along an axis (quantization axis) can only result in the following two states: parallel $S = +\frac{\hbar}{2} = |\uparrow\rangle$ (spin-up) and antiparallel $S = -\frac{\hbar}{2} = |\downarrow\rangle$ (spin-down) aligned spin states. Therefore a transport of spin angular momentum takes place along with the electronic charge current, which gives rise to the spin current. A two channel model is used to understand the two simultaneously emerging currents in which the spin-up and spin-down carriers are considered as non-identical. The model is valid under the assumption that the time interval between two spin flip scattering events is relatively long compared to the time interval between two spin-conserving scattering events [53]. The electric charge current density $\boldsymbol{j}_c$, and the corresponding spin current density $\boldsymbol{j}_s$, can then be written as [54]:

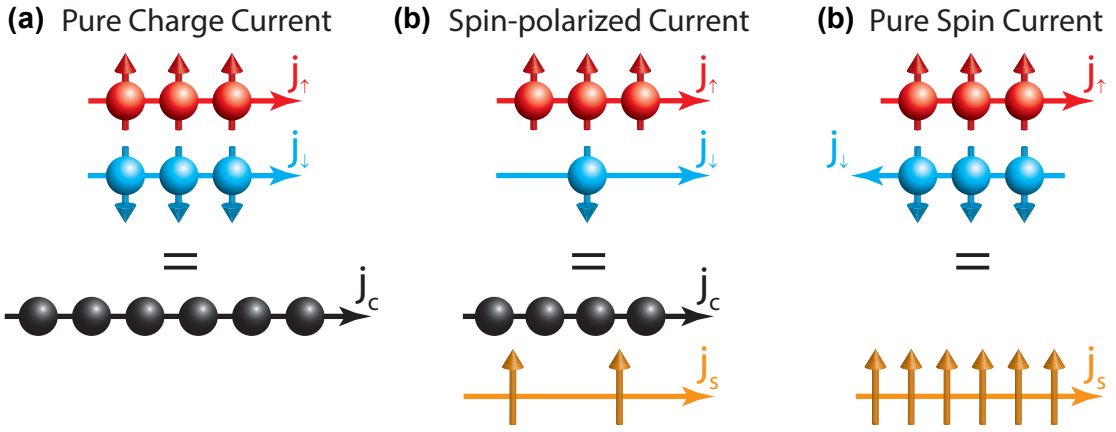

Fig. 2.1: Schematic illustration of charge and spin currents in the two channel model. **(a)** A pure charge current $\boldsymbol{j}_c$ can be represented as the flow of an equal number of up- and down-spin electrons in the same direction. **(b)** A finite spin polarization of the electron system results in a flow of spin angular momentum accompanying the charge current. **(c)** An equal amount of up- and down-spin electrons flowing in opposite directions gives rise to a pure spin current $\boldsymbol{j}_s$. Taken from Ref. [54].

$$\boldsymbol{j}_{\mathrm{c}} = -e(n_{\uparrow}\boldsymbol{v}_{\uparrow} + n_{\downarrow}\boldsymbol{v}_{\downarrow}) = (\boldsymbol{j}_{\uparrow} + \boldsymbol{j}_{\downarrow}), \tag{2.1}$$

$$\boldsymbol{j}_{\mathrm{s}} = \frac{\hbar}{2}(n_{\uparrow}\boldsymbol{v}_{\uparrow} - n_{\downarrow}\boldsymbol{v}_{\downarrow}) = -\frac{\hbar}{2e}(\boldsymbol{j}_{\uparrow} - \boldsymbol{j}_{\downarrow}), \tag{2.2}$$

respectively, with $\boldsymbol{j}_{\uparrow/\downarrow} = -en_{\uparrow/\downarrow}\boldsymbol{v}_{\uparrow/\downarrow}$ accounts for the charge current densities of the two carrier species, where $n_{\uparrow/\downarrow}$ and $\boldsymbol{v}_{\uparrow/\downarrow}$ denote the carrier density and velocity of the particular species, respectively. Charge currents represent the flow of charge with time, therefore the charge current density is represented with unit $\left[\mathrm{Am}^{-2}\right]$. Whereas spin currents represent the transport of spin angular momentum with respect to time hence, the spin current density is represented with unit $\left[\mathrm{Jm}^{-2}\right]$. The conversion factor $-\frac{\hbar}{2e}$ comes in the picture as the fact that the electron is considered as an angular momentum carrier ($\frac{\hbar}{2}$) in $\boldsymbol{j}_{\mathrm{s}}$, whereas it is seen as a charge carrier ($-e$) in $\boldsymbol{j}_{\mathrm{c}}$.

The coupled Eqs. (2.1) and (2.2) can be divided into three cases, as depicted in Fig. 2.1. The first scenario, illustrated in **(a)**, shows a *pure charge current*. In this case, the current densities of both spin $\boldsymbol{j}_{\uparrow}$ state and spin $\boldsymbol{j}_{\downarrow}$ state is equal, therefore producing only a net charge transport with zero angular momentum transport. This is the case for normal (paramagnetic) metals with low spin-orbit coupling (SOC). In case of conducting ferromagnets a *spin-polarized current* is typically observed. As these materials exhibit magnetic ordering, which results in one spin state being more energetically favoured, causing an asymmetry in the density of states at the Fermi level and therefore also in the current densities of the two spin states ($\boldsymbol{j}_{\uparrow} \neq \boldsymbol{j}_{\downarrow}$). The charge current is therefore associated with a spin current, as shown in Fig. 2.1 **(b)**. Equally sized but oppositely directed charge current densities of the two spin states ($\boldsymbol{j}_{\uparrow} = -\boldsymbol{j}_{\downarrow}$) as shown in Fig. 2.1 **(c)**, will lead to a pure flow of angular momentum without accompanying net charge transport - a *pure spin current*. At this point it is important to mention that such a two channel model is intended to give an intuitive understanding of spin currents, but is limited to systems where the spin currents are carried by electrons. References [55–58] provide more general approaches for defining the spin current density.

2.2 Spin Hall Effect

The electrical generation and detection of pure spin currents in this thesis is governed by the spin Hall effect (SHE). The SHE was predicted by Dyakonov and Perel [59] five decades ago and was later theoretically reformulated by Hirsch in 1999 [37]. But the first experimental observation of the effect came in 2004 by Kato et al. [60] nearly thirty years after the original prediction. For conductors with high SOC, an applied charge current $\boldsymbol{j}_{\mathrm{c}}$ will result in spin dependent scattering and will produce a deflection of the flowing electron spins as a consequence of the combined influence of extrinsic impurity scattering [61–63] (i.e. skew- or side-jump-scattering) and intrinsic bandstructure effects [64] (i.e. Berry phase curvature). Subsequently, the oppositely oriented spin states obtain a transverse velocity component in opposite directions, creating a spatial separation and therefore giving rise to a transverse spin current $\boldsymbol{j}_{\mathrm{s}}$, as shown in Fig. 2.2 **(a)**. Satisfying the Onsager reciprocity principle [65], a spin current $\boldsymbol{j}_{\mathrm{s}}$ will also be converted into a charge current $\boldsymbol{j}_{\mathrm{c}}$ as a consequence

of same underlying physics, enabling the inverse spin Hall effect (ISHE), as depicted in Fig. 2.2 **(b)**.

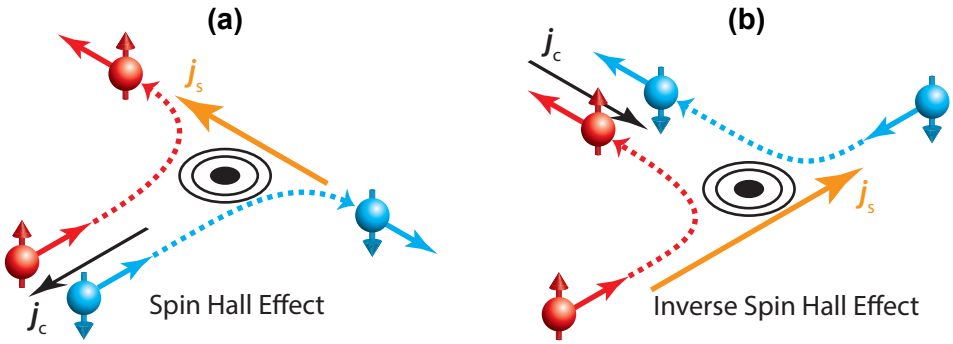

Fig. 2.2: Spin dependent scattering of conduction electrons in paramagnetic materials due to spin-orbit coupling. **(a)** An applied (pure) charge current $\boldsymbol{j}_\mathrm{c}$ gives rise to a transverse (pure) spin current $\boldsymbol{j}_\mathrm{s}$ as a consequence of the spin Hall effect (SHE). **(b)** In a similar fashion, a (pure) spin current $\boldsymbol{j}_\mathrm{s}$ will give rise to a transverse (pure) charge current $\boldsymbol{j}_\mathrm{c}$, owing to the inverse spin Hall effect (ISHE). Taken from Ref. [66].

The conversion efficiency for these processes is the dimensionless quantity called spin Hall angle θ_SH, which tells the efficiency of the charge-to-spin/spin-to-charge conversion. Here, we summarize the SHE and ISHE mathematically with the following equations [67]:

$$\boldsymbol{j}_\mathrm{s} = \theta_\mathrm{SH}\frac{\hbar}{2e}\boldsymbol{j}_\mathrm{c} \times \boldsymbol{s}, \tag{2.3}$$

$$\boldsymbol{j}_\mathrm{c} = \theta_\mathrm{SH}\frac{2e}{\hbar}\boldsymbol{j}_\mathrm{s} \times \boldsymbol{s}, \tag{2.4}$$

respectively.

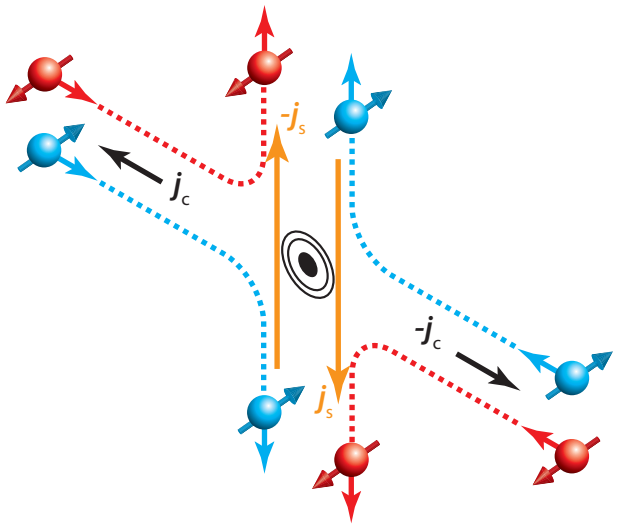

Fig. 2.3: The spin-quantization axis for paramagnetic materials is arbitrary, thus any spin direction with a component perpendicular to the charge current is going to be deflected according to Eq. (2.3). Furthermore, upon reversal of the charge current $\boldsymbol{j}_\mathrm{c}$, the SHE-induced spin current $\boldsymbol{j}_\mathrm{s}$ is reversed as well. The same effect can be achieved by inverting the sign of the spin Hall angle θ_SH. These observations are as well valid for the ISHE, governed by Eq. (2.4).

Heavy metals, such as platinum (Pt), tantalum (Ta) or tungsten (W), have large SOC and thus large spin Hall angles θ_{SH}, whose sign can vary (c.f. Fig. 2.3). For metals like Pt it is 0.1, i.e. 10% of the charge current can be converted into the spin current.

Here, it is important to point out that the SHE effect is not the only effect for generating and detecting the spin currents. Other approaches like nonlocal spin injection [68], spin transfer torque [69], spin pumping [70] and the spin Seebeck effect [71], can also be utilized. But these processes require a bilayer structure, with the spin current being generated in one and subsequently detected in the other material of the bilayer. Whereas SHE has the eminent advantage of generation and detection of spin currents with in a single material [72].

2.3 Spin-Hall Magnetoresistance

Magnetoresistance is the susceptibility of a material to undergo a change in its electrical resistance when placed in an external magnetic field, as firstly discovered by W. Thomson (Lord Kelvin) in 1857 [73]. In the past five decades different magnetoresistance effects like anisotropic [74], giant [4] and tunnel [62] magnetoresistance have been studied and have played an important role in the advancement of data storage technology. These effects mainly rely on the flow of conduction electrons, as they are observed in metallic magnets. Here, the spin Hall magnetoresistance (SMR), reported by "Nakayama, Althammer and coworkers" [6] in NM (normal metal) /MOI (magnetically ordered insulators) bilayers, has shown a fundamentally different magnetoresistance effect, where the conduction electrons of the NM cannot enter the MOI, but still the bilayer resistance reflects the magnetization direction of the interfaced MOI.

In order to understand the underlying physics of the SMR, we will consider a NM/MOI structure as illustrated in Fig. 2.4.

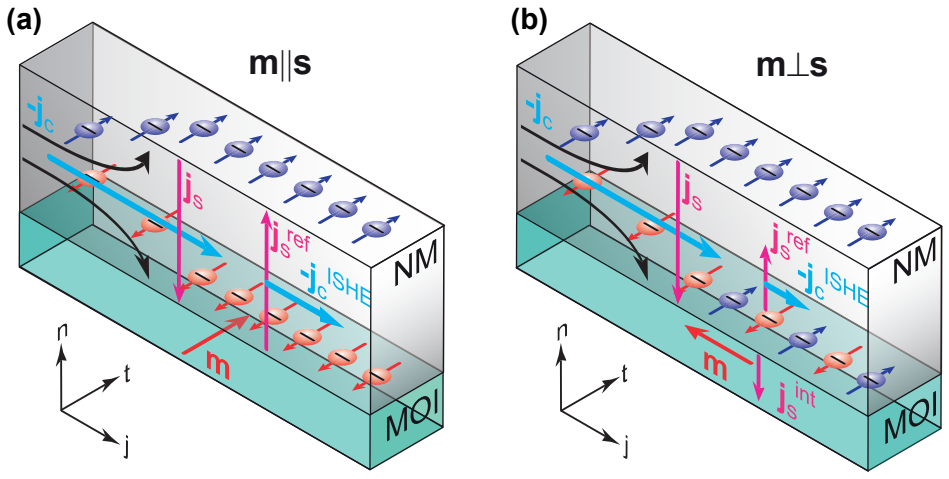

Fig. 2.4: Two limiting cases of SMR in a NM/MOI bilayer. **(a)** For $\boldsymbol{m} \parallel \boldsymbol{s}$, the SHE-induced spin current $\boldsymbol{j}_{\mathrm{s}}$ cannot enter the MOI, thus being reflected as $\boldsymbol{j}_{\mathrm{s}}^{ref}$, therefore resembling the case of isolated NM behavior in absence of the MOI. **(b)** For $\boldsymbol{m} \perp \boldsymbol{s}$, $\boldsymbol{j}_{\mathrm{s}}$ partially enters the MOI, causing a decrease of $\boldsymbol{j}_{\mathrm{s}}^{ref}$, compared to the first case, subsequently resulting in an increase of the resistance. Adapted from Ref. [75].

If a charge current $-\boldsymbol{j}_{\mathrm{c}}$ is applied to the NM in the $\mathbf{j}$-direction, as a consequence of SHE a transverse spin current $\boldsymbol{j}_{\mathrm{s}}$ will be induced. This will flow along $-\mathbf{n}$, with an interfacial

spin polarization $\boldsymbol{s}$ pointing towards $-\mathbf{t}$ for a NM with positive spin Hall angle (θ_{SH}). This will result in a finite spin accumulation $\boldsymbol{\mu}_{\mathrm{s}}$ at the NM/MOI interface, for the cases where the interface is distanced within the same length scale as the spin diffusion length λ_{s}. The spin accumulation is given by $\boldsymbol{\mu}_{\mathrm{s}} = \mu_{\mathrm{s}}^{0}\boldsymbol{s}$, where μ_{s}^{0} [J] denotes the spin chemical potential at the interface. In general, the spin chemical potential arises as a result of spatial separation of opposite spin states $\mu_{\mathrm{s}} = \mu_{\uparrow} - \mu_{\downarrow}$ (where, $\mu_{\uparrow/\downarrow}$ represents the spin chemical potential of a particular spin species) and the gradient of the spin chemical potential represents the driving force for the spin currents. Since we are concerned with a NM/MOI bilayer system, it is important to introduce the magnetization $\boldsymbol{M}$, with $\boldsymbol{m} = \boldsymbol{M}/|\boldsymbol{M}|$ being the resultant magnetization direction of the MOI.

The scenario is depicted in Fig. 2.4 **(a)**, of the parallel alignment of $\boldsymbol{m}$ and $\boldsymbol{s}$, where $\boldsymbol{\mu}_{\mathrm{s}}$ will also be parallelly aligned to $\boldsymbol{m}$, consequently not exerting any spin orbit torque (SOT) on $\boldsymbol{M}$ [8]. As a result, the SHE-induced spin current cannot relax into the MOI, thus prohibiting the flow of any interfacial spin current. This will lead to a complete reflection of the SHE-induced spin current, giving rise to the reflected spin current $\boldsymbol{j}_{\mathrm{s}}^{\mathrm{ref}}$ (note the change of direction), which gets converted into a charge current $-\boldsymbol{j}_{\mathrm{c}}^{\mathrm{ISHE}}$ via ISHE flowing in the same direction as the initial $-\boldsymbol{j}_{\mathrm{c}}$ (c.f. Eq. (2.4)). This case is similar to the case of the isolated NM, therefore it yields the same resistance as of a plain, single layer NM.

In the case depicted in Fig. 2.4 **(b)**, $\boldsymbol{m}$ and $\boldsymbol{s}$ have perpendicular alignment. Now, $\boldsymbol{\mu}_{\mathrm{s}}$ is able to exert SOT on $\boldsymbol{M}$ [76], with a spin current $\boldsymbol{j}_{\mathrm{s,int}}$ flowing across the interface, therefore producing a partial absorption of the spin accumulation $\boldsymbol{\mu}_{\mathrm{s}}$ at the interface. The conduction electrons of the NM undergo a spin-flip scattering process at the interface and transfer a spin angular momentum of $\hbar$ to the magnetization of the MOI [6]. This will lead to a reduction in the reflected spin current $\boldsymbol{j}_{\mathrm{s}}^{\mathrm{ref}}$ as compared to the first case, producing a lower ISHE-induced charge current $-\boldsymbol{j}_{\mathrm{c}}^{\mathrm{ISHE}}$. In totality, we observed a fractional dissipation of the initial charge current $-\boldsymbol{j}_{\mathrm{c}}$ into the MOI for $\boldsymbol{m} \perp \boldsymbol{s}$, which relates to a larger resistance of the NM, known as SMR. The exact amount of the spin accumulation/spin current being absorbed in the MOI is governed by the so-called spin mixing conductance $g^{\uparrow\downarrow}$. It is a complex quantity and represents a measure of the total number of spin-flip scattering taking place at a particular NM/MOI interface when $\boldsymbol{m} \perp \boldsymbol{s}$ and simply can be understood as the total number of open channels for spin transport across interfaces with mutually perpendicular spins [77–80]. The effect can be quantified by writing down the expression for the interfacial spin current [66]:

$$\boldsymbol{j}_{\mathrm{s,int}}(T=0) = \frac{1}{4\pi}\left(g_{\mathrm{i}}^{\uparrow\downarrow} + g_{\mathrm{r}}^{\uparrow\downarrow}\boldsymbol{m}\times\right)(\boldsymbol{\mu}_{\mathrm{s}} \times \boldsymbol{m}), \tag{2.5}$$

with $g_{\mathrm{i}}^{\uparrow\downarrow}$ and $g_{\mathrm{r}}^{\uparrow\downarrow}$ corresponding to the imaginary and real part of $g^{\uparrow\downarrow}$, respectively.

Here we try to provide a simple explanation for this rather complicated expression which is fully discussed in Ref. [66]. Clearly, only for the non-collinear alignment of $\boldsymbol{\mu}_{\mathrm{s}}$ and $\boldsymbol{m}$, both terms in the equation, with respective torques $\propto g_{\mathrm{i}}^{\uparrow\downarrow}$ and $\propto g_{\mathrm{r}}^{\uparrow\downarrow}$ will be finite. Additionally, the second term $\propto \boldsymbol{m} \times (\boldsymbol{\mu}_{\mathrm{s}} \times \boldsymbol{m})$ is governed by the dephasing of spins scattered at the interface due to their precession in the exchange field of $\boldsymbol{m}$. This dephasing results in a loss of transverse spin momentum that is transferred to the magnetic order. Due to incomplete dephasing however, finite transverse momentum will be preserved, therefore directly

exerting torque $\propto \boldsymbol{\mu}_\mathrm{s} \times \boldsymbol{m}$ to the magnetic order. Combined together, the two contributions sum up to Eq. (2.5).

For a phenomenological description, we are primarily interested in the change of the longitudinal resistance of the NM in the bilayer, as a function of the magnetization direction $\boldsymbol{m}$. This can be expressed as [6]:

$$\rho_\mathrm{long} = \rho_0 + \sum_X \rho_{1,X} \left[1 - (\boldsymbol{m}_X \cdot \boldsymbol{t})^2\right] \tag{2.6}$$

$$\rho_\mathrm{trans} = \sum_X \rho_{3,X} \left[(\boldsymbol{m}_X \cdot \boldsymbol{j}\right] \left[\boldsymbol{m}_X \cdot \boldsymbol{t}\right] \tag{2.7}$$

where $\boldsymbol{m}_X$ are the unit vectors of the magnetizations of all sublattices **X** and $\rho_0 = \rho_\perp$ corresponds to the resistivity of the NM itself and ρ_1 and ρ_3 (in Eq. (2.6) and (2.7), respectively) is $\rho_\parallel - \rho_\perp$ i.e. represents the SMR-induced resistivity change ($\rho_\perp$ and $\rho_\parallel$ designate the NM's resistances for $\boldsymbol{j}_\mathrm{c} \perp \boldsymbol{m}$ and $\boldsymbol{j}_\mathrm{c} \parallel \boldsymbol{m}$, respectively). We now define the angle between $\boldsymbol{m}_X$ and $\boldsymbol{j}$ as φ_X such that φ_X = 0° corresponds to $\boldsymbol{m}_X \| \boldsymbol{j}$ and φ_X = 90° corresponds to $\boldsymbol{m}_X \| \boldsymbol{t}$. Such that $\boldsymbol{m}_X \cdot \boldsymbol{j} = \cos\varphi_\mathrm{X}$ and $\boldsymbol{m}_X \cdot \boldsymbol{t} = \sin\varphi_\mathrm{X}$.

For $g_\mathrm{i}^{\uparrow\downarrow} \ll g_\mathrm{r}^{\uparrow\downarrow}$, the resistance change (ρ_1) can be related to the microscopic parameters as [6,8]:

$$\frac{\rho_1}{\rho_0} = \frac{\theta_\mathrm{SH}^2 (2\lambda_\mathrm{s}^2 \rho_\mathrm{NM}) (t_\mathrm{NM})^{-1} g_\mathrm{r}^{\uparrow\downarrow} \tanh(\frac{t_\mathrm{NM}}{2\lambda_\mathrm{s}})}{\frac{h}{2e} + 2\lambda_\mathrm{s} \rho_\mathrm{NM} g_\mathrm{r}^{\uparrow\downarrow} \coth(\frac{t_\mathrm{NM}}{\lambda_\mathrm{s}})}, \tag{2.8}$$

where ρ_NM is the resistivity, t_NM is the thickness and λ_s represents the spin diffusion length of the NM.

In case of ferrimagnetic insulators (FMI), we only have one magnetic sublattice with magnetization $\boldsymbol{m}$ ($|\boldsymbol{m}|$ = 1) oriented parallel to **H** such that $\varphi = \alpha$, equations (2.6) and (2.7) can be expressed as:

$$\rho_\mathrm{long} = \rho_0 + \rho_1 \left[1 - \sin^2\alpha\right] = \rho_0 + \rho_1 \cos^2\alpha = \rho_0 + \frac{\rho_1}{2} + \frac{\rho_1}{2}\cos 2\alpha, \tag{2.9}$$

$$\rho_\mathrm{trans} = \rho_3 \sin\alpha \cos\alpha = \frac{\rho_3}{2} \sin 2\alpha, \tag{2.10}$$

As the work done during this thesis mainly deals with the antiferromagnets, here it is important to discuss the equations (2.6) and (2.7) in the context of antiferromagnetic insulators (AFI). For the case of a single antiferromagnetic domain with two sublattices **X** = 1, 2 and no effective canting, we consider $\boldsymbol{m}_1 = -\boldsymbol{m}_2 \perp \mathbf{H}$ ($|\boldsymbol{m_1}| = |\boldsymbol{m_2}| = 1$) [45,48], resulting in $\varphi_1 = \alpha + 90°$ and $\varphi_2 = \alpha - 90°$. Such that $\rho_{1,1} = \rho_{1,2} = \frac{\rho_1}{2}$ and $\rho_{3,1} = \rho_{3,2} = \frac{\rho_3}{2}$ we obtain

$$\rho_\mathrm{long} = \rho_0 + \rho_1 \left[1 - \cos^2\alpha\right] = \rho_0 + \rho_1 \sin^2\alpha = \rho_0 + \frac{\rho_1}{2} - \frac{\rho_1}{2}\cos 2\alpha, \tag{2.11}$$

$$\rho_\mathrm{trans} = \frac{\rho_3}{2} \left[(-\sin\alpha)\cos\alpha + \sin\alpha(-\cos\alpha)\right] = -\frac{\rho_3}{2}\sin 2\alpha, \tag{2.12}$$

As a consequence of the equations (2.9), (2.10), (2.11) and (2.12) we expect a qualitative difference of the angle dependent magnetoresistance (ADMR) between FMI and AFI; a

phase shift of 90° with respect to the angle α for the in-plane rotations of the externally applied field **H**.

In our experiments we manipulate the magnetic sublattices with an externally applied magnetic field and detect the corresponding resistivity changes. In case of FMI as MOI we can reorient the magnetisation **M** with the externally applied field **H**. The sublattices orient (anti) parallel to **H** for sufficiently high magnitudes of the applied field. Here we would introduce an angle α between **-J**$_q$ and **H** to define the direction of **H** (Fig. 2.5). Such that α = 0° (**H**$\|$**j**) (see Fig. 2.5**(a)**) corresponds to the case of relaxation of the spin current into the MOI hence, a higher resistivity ρ_{long}. For α = 90° (**H**$\|$**j**) where spin current is reflected and gets transformed into charge current via ISHE ultimately resulting in a lower resistivity (Fig. 2.5**(b)**), when compared to the previous case.

For the case of AFI as MOI, we expect a perpendicular orientation of the magnetic sublattices $\mathbf{M}_{1,2}$ with respect to **H** per magnetic domain, which is multiply reported in the literature [44–48]. As illustrated in the Fig. 2.5**(c, d)** for the monodomain case, the relaxation and reflection of the spin currents is shifted by a phase of 90° from the FM case (Fig. 2.5**(a, b)**). In summary, α = 0° now corresponds to the spin current reflection case with low ρ_{long} and α = 90° to the spin relaxation case with high ρ_{long}.

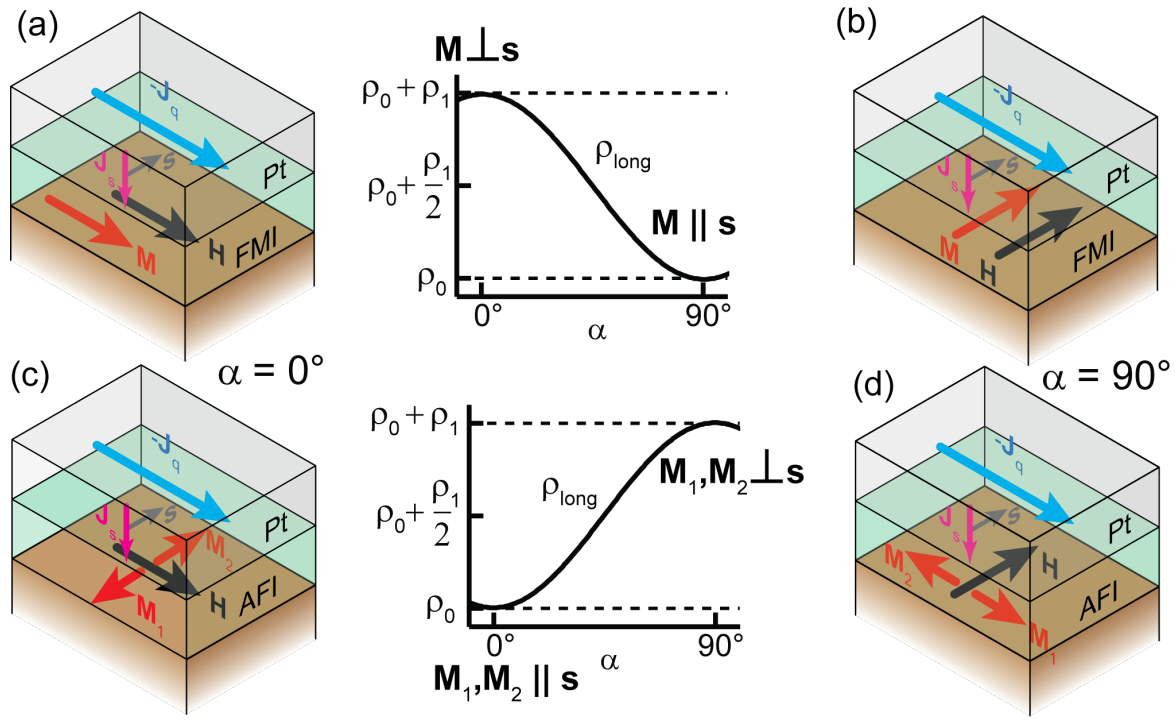

Fig. 2.5: The charge current (J_{q}) is transformed into a spin current (J_{s}) by SHE with a spin polarisation **s** at the Pt | MOI interface (in **(a)** and **(b)** MOI is a FMI; in **(c)** and **(d)** MOI it is an AFI). For perpendicular orientation between the magnetisation **M** in the FMI **(a)** or $\mathbf{M}_{1,2}$ in the AFI **(d)** to **s**, spin transfer torque with spin relaxation is possible and causes a higher resistivity ρ_{long} (measured along J_{q}) then for **M**$\|$**s (b)**, or $\mathbf{M}_{1,2}\|$**s (c)**. ρ_0 is the resistivity of the bare Pt electrode and ρ_1 is the SMR amplitude [8].

At this point the phase of the SMR is well understood in different magnetically ordered insulators but the amplitude is still not very well understood and is a matter of debate. The amplitude is governed by real part of spin mixing interface conductance $g_{\text{r}}^{\uparrow\downarrow}$ as discussed in the Eq. (2.8) and parameters on which this factor depends is still not very clear. We took

the SMR amplitude data from the experiments done at our institute and plotted the SMR oscillations (Fig. 2.6 **(a)**) with the in plane angle α. The extracted amplitude is plotted as a function of spin density of the system in Fig. 2.6 **(b)**. We see linear dependence on the spin density of the system, in order to further verify this hypothesis we need more data of systems with different spin densities.

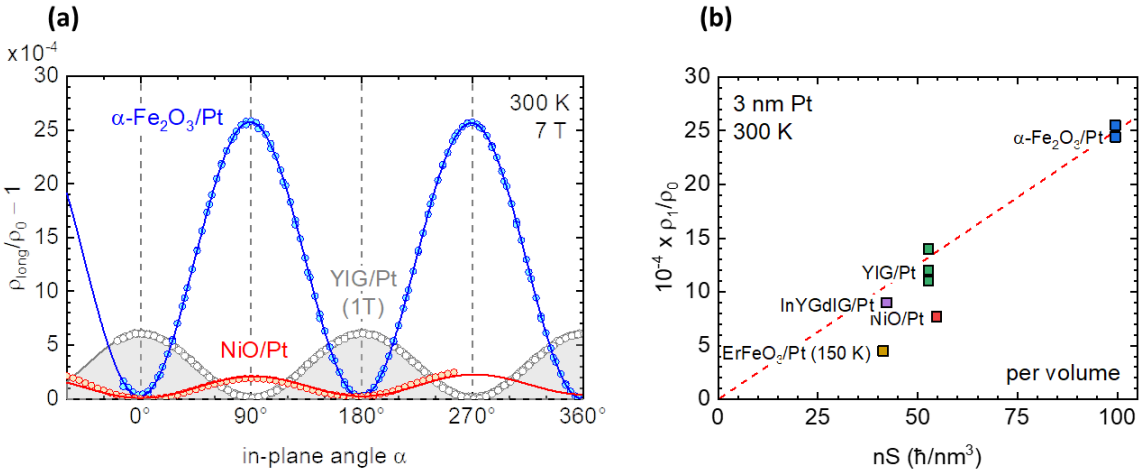

Fig. 2.6: The SMR oscillation for different systems is depicted as a function of in plane angle α in **(a)** and **(b)** shows the extracted amplitude as a function of spin density per unit volume of the system [7, 46, 47, 52].

3 Experimental Details

In the first part of this chapter, we present a brief overview on different iron oxides. We have done a characterisation based on iron ions present in the oxide i.e. Fe^{3+} alone, combination of Fe^{3+}/Fe^{2+} or Fe^{2+}.In the second part of the chapter we present the experimental techniques used in the framework of this thesis. We start from the fabrication of the epitaxial thin films using pulsed laser deposition (PLD) and in-situ deposition of metal electrodes using electron beam evaporation (EVAP). Then the structural and magnetic characterisation techniques, X-ray diffraction and SQUID magnetometry are discussed. And finally optical lithography and superconducting magnet cryostat and different rotational geometries used for magnetotransport measurement is discussed.

3.1 Different Iron Oxides

The iron-oxygen system exists in several different crystal structures and oxidation states. Hematite ($\alpha-Fe_2O_3$) and wustite (FeO) are antiferromagnetic whereas maghemite ($\gamma-Fe_2O_3$) and magnetite (Fe_3O_4) are ferrimagnetic. A list of different iron oxides with their crystal structure and magnetic properties is given in table 3.1.

Iron oxide	Crystal structure	Lattice constant (nm)	Magnetic ordering	Ordering temperature (K)
$\alpha-Fe_2O_3$	Hexagonal	a = 0.504, c = 1.375	Antiferromagnetic	950
$\beta-Fe_2O_3$	Cubic	a = 0.940	Antiferromagnetic	119
$\gamma-Fe_2O_3$	Cubic	a = 0.838	Ferrimagnetic	950
$\epsilon-Fe_2O_3$	Orthorhombic	a = 0.510, b = 0.878, c = 0.946	Ferrimagnetic	495
Fe_3O_4	Cubic	a = 0.839	Ferrimagnetic	858
FeO	Cubic	a = 0.430	Antiferromagnetic	198

Tab. 3.1: List of different iron oxides with their crystal structure and magnetic properties

3.1.1 Iron (III) oxide

With chemical formula of Fe_2O_3, iron (III) oxide can show four different crystal structures/ polymorphs: alpha, beta, gamma and epsilon. The hexagonal and cubic phases, also called as alpha (α) and gamma (γ) phase are well-studied and extensively applied in the industry as magnetic and red dye materials. Whereas epsilon (ϵ) and beta (β) are rare phases. Studies have shown epsilon phase exhibiting large coercive field [81]. $\epsilon-Fe_2O_3$ has orthorhombic structure (a=0.510, b=0.878, c=0.946 nm [82])and $Pna2_1$ space group, with a ferrimagnetic transition temperature T_c of 495 K [81]. $\beta-Fe_2O_3$ has bixbyite-type cubic structure ($Ia\bar{3}$) with lattice constant a= 0.940 nm. It is an intermediary metastable phase; at temperatures close to 600 °C it transforms easily into $\alpha-Fe_2O_3$, making it difficult to obtain in monophase [83]. It exhibits antiferromagnetic properties with a Neel temperature of 119 K [81].

$\alpha-Fe_2O_3$ (also known as hematite) is the most stable iron oxide in air, under ambient conditions [84]. It has a hexagonal crystal structure with lattice parameters $a = 0.504$ nm and $c = 1.375$ nm. It is an electrical insulator and exhibits antiferromagnetic ordering at

temperatures below T_N = 950 K above which it becomes paramagnet [85]. Bulk Hematite undergoes a first order spin-reorientation transition at 263 K known as Morin transition (T_M). This transition is characterized by a sign change of the uniaxial magnetic anisotropy, resulting in a transition from a magnetic easy (0001)-plane above T_M to a magnetic easy (0001)-axis below T_M. Below T_M the moments in two sublattices are exactly antiparallel and are aligned along the hexagonal c axis. Above which the anisotropic Dzyaloshinskii-Moriya superexchange interaction leads to a small canting of moments lying in the basal plane (0001) resulting in a weak net moment [84]. The existence of Morin transition in $\alpha-Fe_2O_3$ thin films is not always confirmed and is a matter of debate [85].

Maghemite, $\gamma-Fe_2O_3$ is a ferrimagnetic insulator with an inverse spinel structure similar to magnetite but has a defective lattice with one ninth of the Fe positions in the lattice being vacant. Maghemite cubic unit cell has a lattice constant, $a = 0.838$ nm [86, 87]. The cations completely occupy all the tetrahedral sites, and the remaining cations are randomly distributed in octahedral sites [88]. It exhibits a high Neel temperature of 950 K [89].

3.1.2 Iron (III) / (II) oxide

Magnetite (Fe_3O_4) is a well-known ferrimagnetic material with a high Curie temperature of 858 K [90]. In particular Fe_3O_4 thin films attracted great attention for application in spintronic devices due to the predicted, half-metallic character and high spin polarisation (100%) by band structure theory [91]. It has an inverse spinel crystal structure with a lattice parameter of $a = 0.839,$ nm and Fd3m space group and shows a first order so-called Verwey transition from cubic inverse spinel to monoclinic at 120 K [92]. The cubic unit cell of magnetite contains 24 iron cations (8 Fe^{2+} & 16 Fe^{3+}) and 32 oxygen anions. The iron ions are distributed in-between the oxygen interstices, 16 octahedral (B) sites are equally occupied by Fe^{3+} and Fe^{2+} ions, whereas tetrahedral (A) sites are only occupied by the Fe^{3+} ions. The individual A and B sublattices are ferromagnetically ordered but due to super exchange with respect to each other they are antiferromagnetically coupled [93]. Magnetite has significantly lower resistivity compared to maghemite and transforms into $\gamma-Fe_2O_3$ with further oxidation along with the creation of iron vacancies in the octahedral sites [89]. When compared to other iron oxides FeO and Fe_2O_3, magnetite has lower resistance at room temperature due to rapid and continuous hopping of electrons between the Fe^{3+} and Fe^{2+} cations of the B site [92].

3.1.3 Iron (II) oxide

FeO (wüstite) has a cubic rock-salt lattice (with lattice constant $a = 0.430$ nm [94]) in which Fe^{2+} (cations) and O^{2-} (anions) are alternatively arranged along the [111] direction [95]. A key characteristic of this phase is the presence of non-stoichiometry Fe_yO with y varying from 0.88 to 0.96 [96]. This cation deficiency is accommodated by the formation of octahedral iron vacancies and a small number of tetrahedral iron (III) interstitials. It exhibits antiferromagnetic ordering below a Neel temperature of 198 K, but the exact Neel temperature (T_N) depends on the value of y [97]. Neutron diffraction experiments show that below T_N, the magnetic moments of the Fe^{2+} iron ions form ferromagnetic (111) sheets. Where the moments point alternatively up and down perpendicular to the (111) planes

(Fig. 3.1)resulting in antiferromagnetic coupling of iron spins along the [111] direction [96]. The antiferromagnetic ordering also introduces a rhombohedral distortion along the [111] axis. Other metal monoxides such as MnO, CoO and NiO also show similar structural and magnetic characteristics [95].

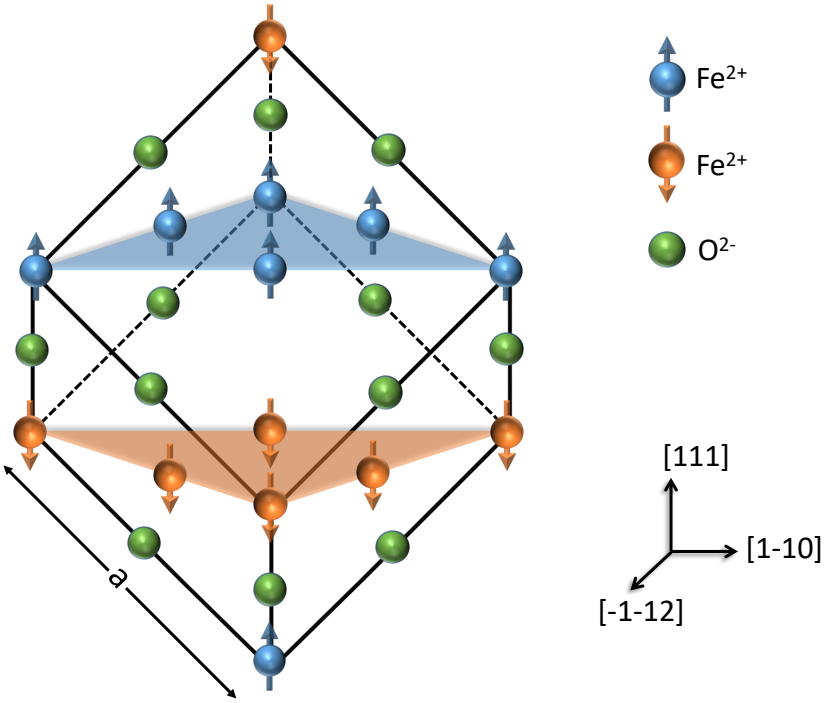

Fig. 3.1: FeO crystal structure. The green oxygen ions (O^{2-}) occupy the edge centres whereas the corners and the face centres are occupied by Fe^{2+} ions. The red and blue triangles show the {111} planes where Fe^{2+} spins point perpendicular to the plane.

3.2 Experimental setup

3.2.1 Pulsed Laser Deposition (PLD)

The FeO thin film deposition on single crystalline sapphire and MgO substrates was done using Pulsed Laser Deposition (PLD), as this physical vapor deposition technique is a very effective and flexible method for epitaxial thin film growth. The PLD process itself takes place in vacuum chamber and can be divided into three parts, which take place at each laser pulse: (i) target material ablation, vaporization, and ionisation (ii) transport to substrate and (iii) deposition and growth of thin film on the substrate.

As depicted in Fig. 3.2 the first part of the process uses a KrF UV excimer laser (248 nm, max.repetition rate 10 Hz), to ablate the polycrystalline target. A five-lens telescope assembly is used to focus the pulses on a polycrystalline target (laser fluence $0.5-5\,\mathrm{J/cm^2}$). When the laser hits the target the conversion of electromagnetic energy of laser radiation takes place, first into electronic excitation followed by a transformation into thermal, chemical and even mechanical energy [99]. In the second step of the process, high energy density at the target surface results in plasma plume generation that expands towards the substrate. This process adiabatically cools down the plasma to temperatures around 3000-5000 K. The angular distribution of the plasma plume can be described by a $\cos^n(\theta)$ function.

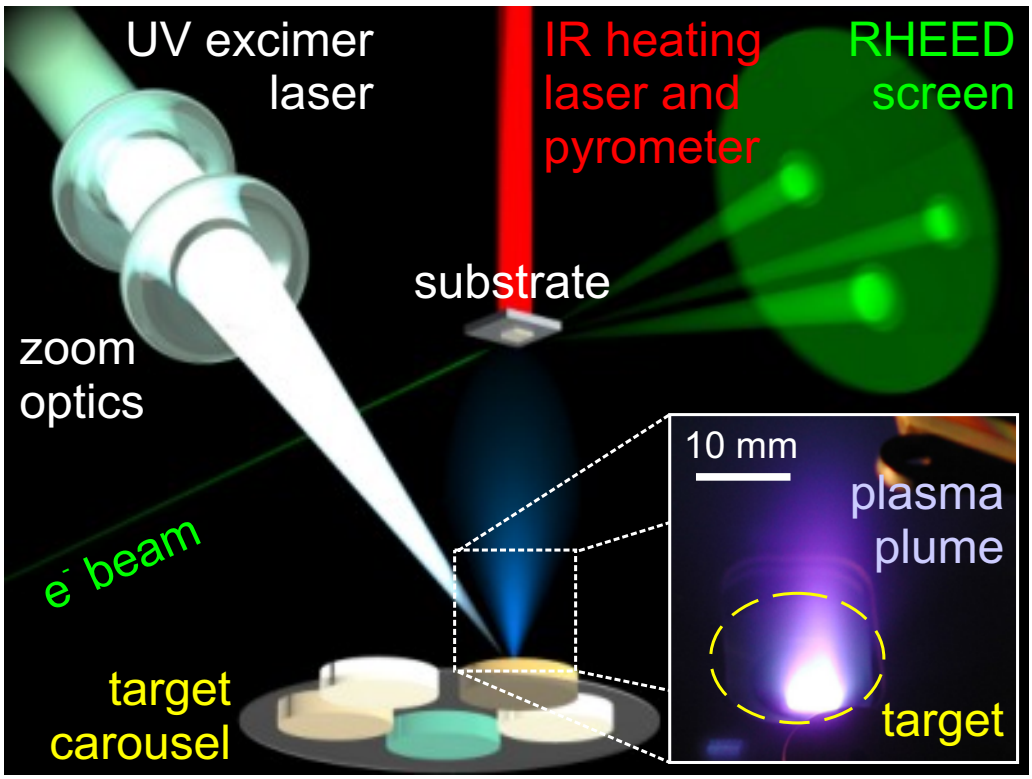

Fig. 3.2: Pulsed Laser deposition setup at Walther Meissner Institute. Adapted from [98]

In the final part of the PLD process, thin film deposition takes place on the substrate. The step itself is a combination of multiple microscopic processes, such as adsorption, diffusion and desorption of adatoms.

The substrate temperature is maintained at the desired, elevated value using a contactless infrared (IR) laser heating system (140 W, 940 nm) from the backside. The temperature is measured with a pyrometer and computer-controlled. During the growth process, an automated system regulates the turbo pump valve to maintain a stable pressure between 10^{-4} and 1 mbar inside the chamber. Different process gases (Ar, O_2, N_2, N_2/H_2, Ar/H_2) can be used for the background atmosphere.

3.2.2 Electron bean evaporation (EVAP)

Electron beam evaporation which is also a physical vapor deposition technique was employed to deposit in-situ metallic electrodes on top of the oxide thin films. A filament is used to generate an intense beam of electrons that are further accelerated by an electric field and are finally focused by a magnetic field on to the target material. This electron beam will heat the target material to its melting point until the surface atoms have enough energy to leave the surface and evaporate, as shown in Fig. 3.3 The thermal energy is low therefore; a vacuum is required such that the mean free path is grater then the separation between the target and the substrate. During the whole process, an oscillating quartz crystal is used to monitor the growth rate and permits to stop the process when the desired thickness is reached [85].

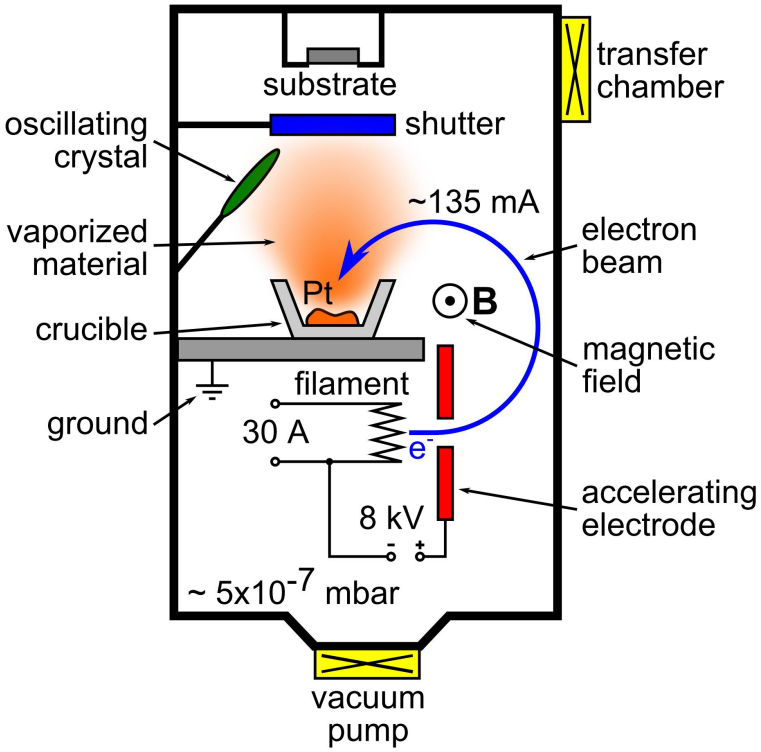

Fig. 3.3: Schematic of the EVAP setup used. Adapted from [75]

3.2.3 X-ray Diffraction

In the course of this thesis, x-ray diffraction measurements were carried out using a Bruker D8 Discover four-circle x-ray diffractometer. A copper target is used to produce $Cu - K_{\alpha 1}$ X-rays of wavelength λ = 0.15406 nm. The X-rays are monochromatized by a Goebel mirror and a Ge(002) monochromator and subsequently diffracted from the sample. Constructive and destructive interference of the X-ray beam takes place at the lattice planes, the diffraction angle theta can be used to determine the distance between them (d_{hkl}) using Bragg's law:

$$n\lambda = 2d_{hkl}\sin\theta \ , \tag{3.1}$$

When the above equation is fulfilled we get a constructive interference and that is seen as maximum in the intensity plot. Where n is the order of the diffraction. For the determination of the out-of-plane lattice constant a 2θ-ω-scan is carried out. The sample is scanned with a proportional 2θ-ω relation. In plane lattice constants are determined using reciprocal space maps, which consist of several 2θ-ω scans with different 2θ-ω relations.

For a cubic crystal system the following d_{hkl} relation is used to determine the lattice constant a:

$$d_{hkl} = \frac{a}{\sqrt{h^2 + k^2 + l^2}} \ . \tag{3.2}$$

h, k, l are the Miller indices for the three directions in reciprocal space.

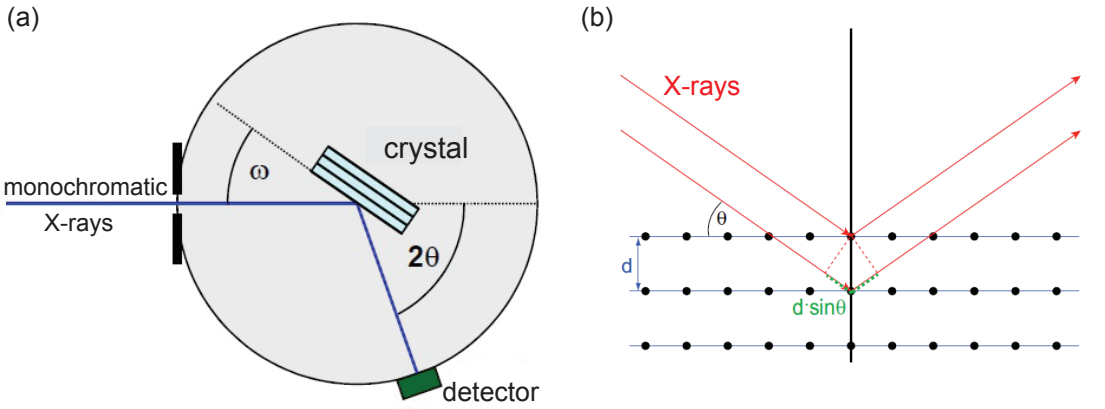

Fig. 3.4: Schematic representation of the X-ray beam path of the Bruker AXS D8 Discover setup used. Adapted from [85]

For determination of the thickness and roughness of the layer stack, X-ray reflectometry is used. The geometry is same as in case of 2θ-ω scans done earlier. However, the 2θ range is restricted to small angles near gracing incidence between $0.5°$ and $5°$ to allow the X-ray diffraction from the surface and the interface instead of the lattice planes.

3.2.4 Superconducting quantum interference device (SQUID) magnetometry

To determine the magnetization of the thin films, superconducting quantum interference device (SQUID) magnetometry was employed. The SQUID magnetometer measures the magnetic moment of the sample as a function of either applied field or temperature.

As depicted in Fig. 3.5(a), the sample is glued with the diamagnetic rubber cement 'Marabu FIXOGUM' in a diamagnetic plastic straw which is moved up and down in a second order gradiometer. This is the name of the measuring geometry of the superconducting pick-up coil, to suppress the pickup of linear field inhomogeneities and noise produced by interfering field gradients over the length of the gradiometer. As the straw passes all 4 loops it induces no signal, whereas the magnetic flux of the sample creates a current which is transformed by a RF-SQUID into a voltage curve (Fig. 3.5(b)). As a result the SQUID converts the flux signal-to-voltage signal with an extreme sensitivity of 10^{-8} emu ($= 10^{11}\mathrm{Am}^2$)

The software fits the curve and determines the absolute magnetic moment m in the direction of the magnetic field. We then have to subtract the signal of the substrate and determine the magnetization of the sample by dividing by its volume V.

$$M = \frac{m}{V} \tag{3.3}$$

We calculate V of the thin film by multiplying its thickness from X-ray reflectometry (Sec. 3.2.3) with the surface area, obtained from a microscope image.

The SQUID magnetometer MPMS XL-7 manufactured by Quantum Design with its superconducting magnet can produce magnetic fields between -7 T and 7 T and the cooling system permits to vary the temperature between $1.8\,\mathrm{K}$ and $400\,\mathrm{K}$.

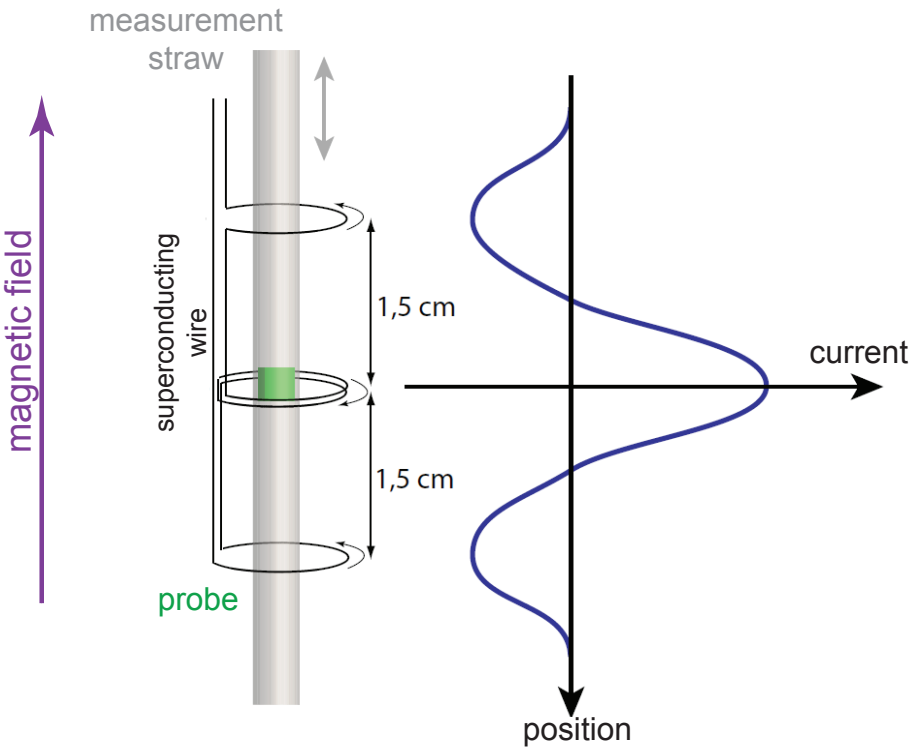

Fig. 3.5: Sketch of the gradiometer of the SQUID magnetometer and the typically measured signal. Adapted from [85]

3.2.5 Lithography

The Hall bar mesa structures for magnetotransport measurements were patterned using the PicoMaster 200 laser writer from 4PICO, which uses an UV laser to write the structures. Before putting the sample in the laser writer a photoresist was spin coated onto the film. Then the pattern shown in the Fig. 3.6 was written, further the photoresist was developed using AZ-726 MIF developer for 60 seconds. Later Ar-ion milling was used to remove the uppermost layer of the film in the areas that are not protected by photoresist to reveal the structure.

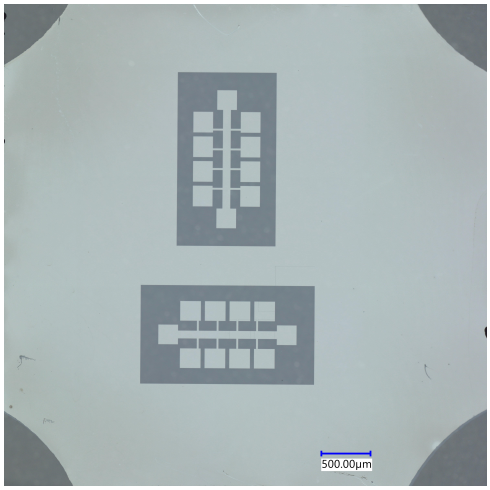

Fig. 3.6: Optical microscope image of the Hall bar mesa structure, taken after Ar ion milling

3.2.6 Superconducting magnet cryostat

For the magnetotransport measurements a cryogenic system from Oxford Instruments was used. The setup allows the determination of resistance as a function of the magnetic field magnitude, its direction, and the temperature. The cryostat hosts a superconducting split coil magnet system that can produce fields up to 7 T. The cryostat utilizes a liquid He cooling system and can perform measurements between 2 K and 300 K. We apply magnetic field magnitudes in horizontal direction up to 7 T. The dipstick with the sample is inserted vertically and can be rotated around its axis between $-20°$ and $380°$. The sample can be mounted with its surface horizontally or vertically and allows so in plane (ip) and out of plane (oop) rotations, respectively. For FeO we measured the ip and oop rotation with this system. For the measurements performed in this thesis, we patterned the samples into a Hall bar structure as depicted in Fig. 3.7.

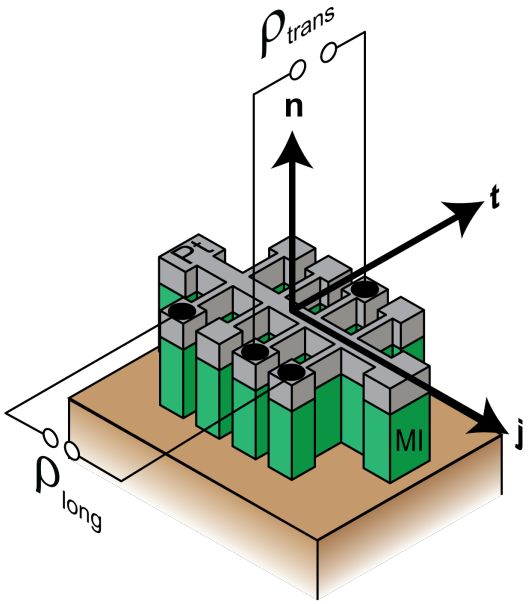

Fig. 3.7: Measurement geometry of a metal insulator (MI) | Pt bilayer, patterned into a Hall bar structure via photolitography with current direction *j*, transverse axis *t* and normal direction *n*. ρ_{long} is determined along *j*, ρ_{trans} along *t* by measuring the voltage drop while applying a current along *j*

This permits us to apply a current along the *j* direction (Fig. 3.7). This allows a easy measurement of the longitudinal resistivity (ρ_{long}) along the *j* and a transverse resistivity (ρ_{trans}) along *t* (as shown in Fig. 3.7). The rotation of applied field **H** in the Hall bar plane is an "*ip*"rotation (Fig. 3.8(**a**)), in a plane perpendicular to *j* an "*oopj*"(Fig. 3.8(**b**)) and perpendicular to *t* an "*oopt*"rotation (Fig. 3.8(**c**)).

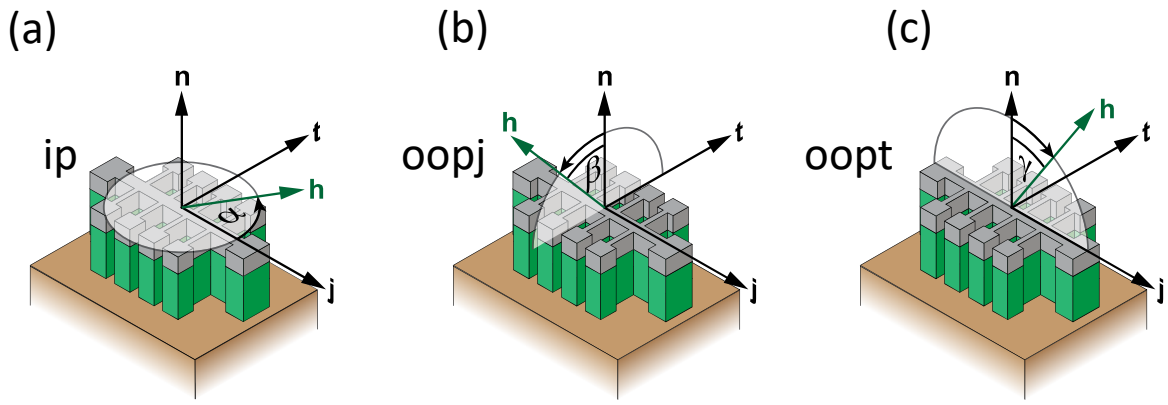

Fig. 3.8: Definition of the rotation planes of the external magnetic field with unit vector h. (**a**) in the Hall bar plane (ip). (**b**) in a plane perpendicular to the current direction j (oopj). (**c**) in a plane perpendicular to the transverse direction t (oopt).

3.2.7 Sensitive transport measurements via DC current switching method

The DC current switching method was used for the SMR measurements of the device with four point connections as shown in Fig. 3.7. The charge current applied for the four point measurement produces Joule heating in the Pt, resulting in additional thermal voltages, for instance due to spin Seebeck effect [100–102]. In order to disentangle the thermal (V_{therm}) and resistive voltage response (V_{res}), we use a DC current switching (reversal) method (or "delta method"), which comprised of applying DC currents of positive (+J_c) and negative (-J_c) polarity subsequently to the device. Simultaneously, the corresponding voltage drops V(+J_c) and V(-J_c) are recorded [103]. This allows us to differentiate between the contributions which depend on the current direction, the resistive or higher order effects which are uneven in J_c i.e. their contribution switch sign upon polarity change

$$V_{\mathrm{res}} = \frac{V(+J_{\mathrm{c}}) - V(-J_{\mathrm{c}})}{2} \tag{3.4}$$

from the thermal contributions which are proportional to the quadratic or higher order even terms in J_c i.e. their contributions are insensitive to the polarity change

$$V_{\mathrm{therm}} = \frac{V(+J_{\mathrm{c}}) + V(-J_{\mathrm{c}})}{2} \tag{3.5}$$

In addition to disentangling the thermal and resistive contributions, the current switching method also allows to reach higher sensitivity in resistivity measurements. We used a current switching N_{switch} = 4 times for each magnetic field orientation and magnitude. This helped us to improve the signal to noise ratio in the ADMR measurements while calculating the average of V_{res} and V_{therm} separately. Hereby, we were able to correct thermal drifts which can arise on the time scales of seconds, such thermal fluctuations can arise during the rotations of the dipstick in the He exchange gas of the cryostat. As for the instruments, we used Keithley 2400 Sourcemeters to feed currents through the devices and Keithley 2182 Nanovoltmeters for measuring the voltage drop.

4 Spin Hall Magnetoresistance in NM | FeO Heterostructures

In this chapter we present the magnetoresistance measurements in Pt | FeO heterostructures grown on single crystalline sapphire and MgO substrates. Before presenting the angle-dependent magnetoresistance (ADMR) and field dependent measurements we first discuss the growth of FeO thin films as there are not many reports on FeO thin film growth [89, 96, 97, 104, 105] as it is not the most stable iron oxide in atmosphere and is challenging to grow.

4.1 Fabrication of Pt | FeO thin films

The fabrication of FeO films was done in four batches in order to obtain the optimised parameters. The first batch of films were prepared on (0001)-oriented sapphire substrates in the pure argon atmosphere. The second batch was prepared on (001)-oriented MgO substrates in formiergas (5% H_2 and 95% N_2) atmosphere. The third and forth batches were prepared on (0001)-oriented sapphire and (001)-oriented MgO substrates in formiergas atmosphere with N_2 gas being replaced by Ar. For every batch we prepared temperature, pressure and thickness series to find the optimised parameters. In the following sections 4.1.1 and 4.1.2 we discuss the optimised growth parameters on sapphire and MgO substrates, respectively. A short summary of samples prepared during this work can be found in appendix (A).

4.1.1 On sapphire substrate

FeO thin films on sapphire substrates were grown using PLD using $\alpha-Fe_2O_3$ target with a laser fluence of 2.5 J/cm^2 and 2 Hz repetition rate at $390\,^{\circ}\mathrm{C}$ in $25\,\mu\mathrm{bar}$ of formiergas (5% H_2 and 95% Ar) atmosphere. A thickness of 10 nm was obtained with 10,000 pulses. Further a 3.8 nm thick Pt electrode was deposited in-situ via EVAP.

The (111)-oriented FeO films were grown on (0001)-oriented Al_2O_3 substrates. Sapphire has a hexagonal crystal structure with lattice constants $a = 0.4763$ nm and $c = 1.3003$ nm. During the epitaxial growth the oxygen sublattice continues. Therefore to calculate the lattice mismatch ϵ we consider the separation between two oxygen atoms in the (0001) plane of the Al_2O_3 ($\delta_{O,Al_2O_3} = 0.275$ nm [98]) and in the (111) plane of FeO ($\delta_{O,FeO} = a_{FeO}/\sqrt{2} = 0.304$ nm) of

$$\epsilon_0 = \frac{\delta_{\mathrm{O,FeO}} - \delta_{\mathrm{O,Al_2O_3}}}{\delta_{\mathrm{O,Al_2O_3}}} = 10.5\,\% \tag{4.1}$$

Hence, we expect a relaxed growth of FeO on sapphire substrate.

In order to characterise the crystallographic structure of our samples X-ray diffraction was employed. For the out of plane $2\theta - \omega$ scan we only observe reflections which correspond to either film or substrate (Fig. 4.1). The expected (000l) reflections from the Al_2O_3 substrate were seen also, (hkl) reflections with (h=k=l) from the FeO thin film, evidenced that FeO[111] | | Al_2O_3[0001]. In addition, a broad feature from the Pt top electrode was observed, since the cubic Pt of lattice constant $a = 0.3920$ nm [106] shows a (111) reflection at $39.80°$. Presence of no secondary phases was detected. Using the FeO reflection at θ_{111} =18.17° and via Bragg's law (Eq.(3.1)), we calculated the distance between the FeO {111} planes to $d_{\mathrm{FeO}} = 0.246$ nm. The calculated value of distance between {111} planes is

$d_{\mathrm{FeO,literature}} = d_{\mathrm{FeO}}/\sqrt{3} = 0.248$ nm, using the literature values of the FeO lattice constant. The lower value of distance between the planes for our sample can be attributed to Fe^{2+} cation vacancies, which reduces the lattice size and hence the inter-planner distance.

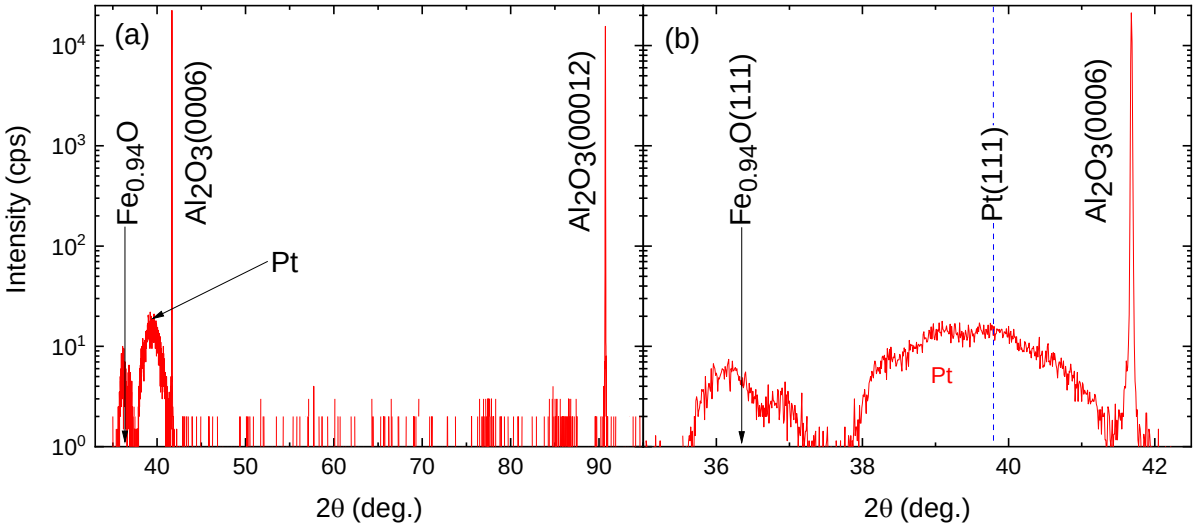

Fig. 4.1: X-ray diffraction diagram. **(a)** and **(b)** show the $2\theta - \omega$ scans of the FeO films on the $Al_2O_3(0001)$ substrate. Here we see (0006) and (00012) reflections of the Al_2O_3 substrate at $2\theta = 41.65°$ and $90.67°$. The (111) reflection from $Fe_{0.94}O$ is seen at $2\theta = 36.34°$. We see the Pt electrode feature around $2\theta = 40°$, the (111) reflection from the bulk Pt is expected at $39.80°$ (dashed blue line in **(b)**). The intensities are given in counts per second.

For the determination of the layer thickness we apply X-ray reflectometry from $2\theta = 0.5°$ to $5°$ (Fig. 4.2). The larger oscillations with large period originate from the top Pt electrode and the small oscillations with small period are given by the FeO film. Using the simulation of experimantal data from the LEPTOS software, we obtained a thickness of $t_{\mathrm{FeO}} = 10$ nm and $t_{\mathrm{Pt}} = 3.8$ nm and low rms surface roughness of 0.8 nm.

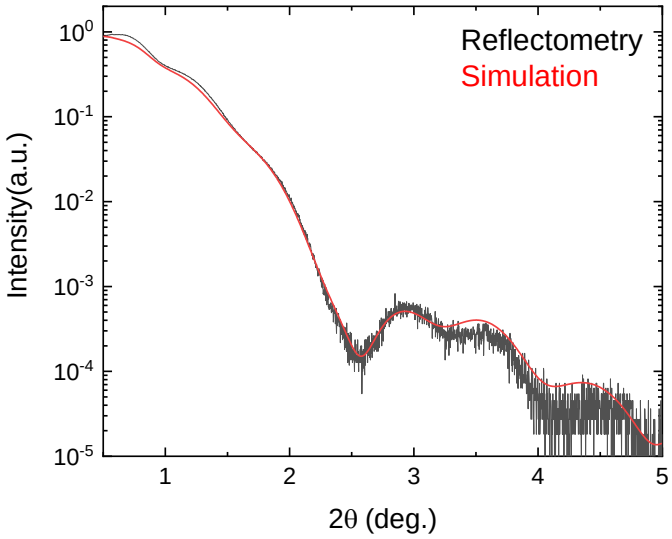

Fig. 4.2: X-ray reflectometry of Pt | FeO(111) bilayer on sapphire substrate. Red curve is the simulated curve on black experimental curve. The simulation is done using the LEPTOS software. The intensity is given in arbitrary units.

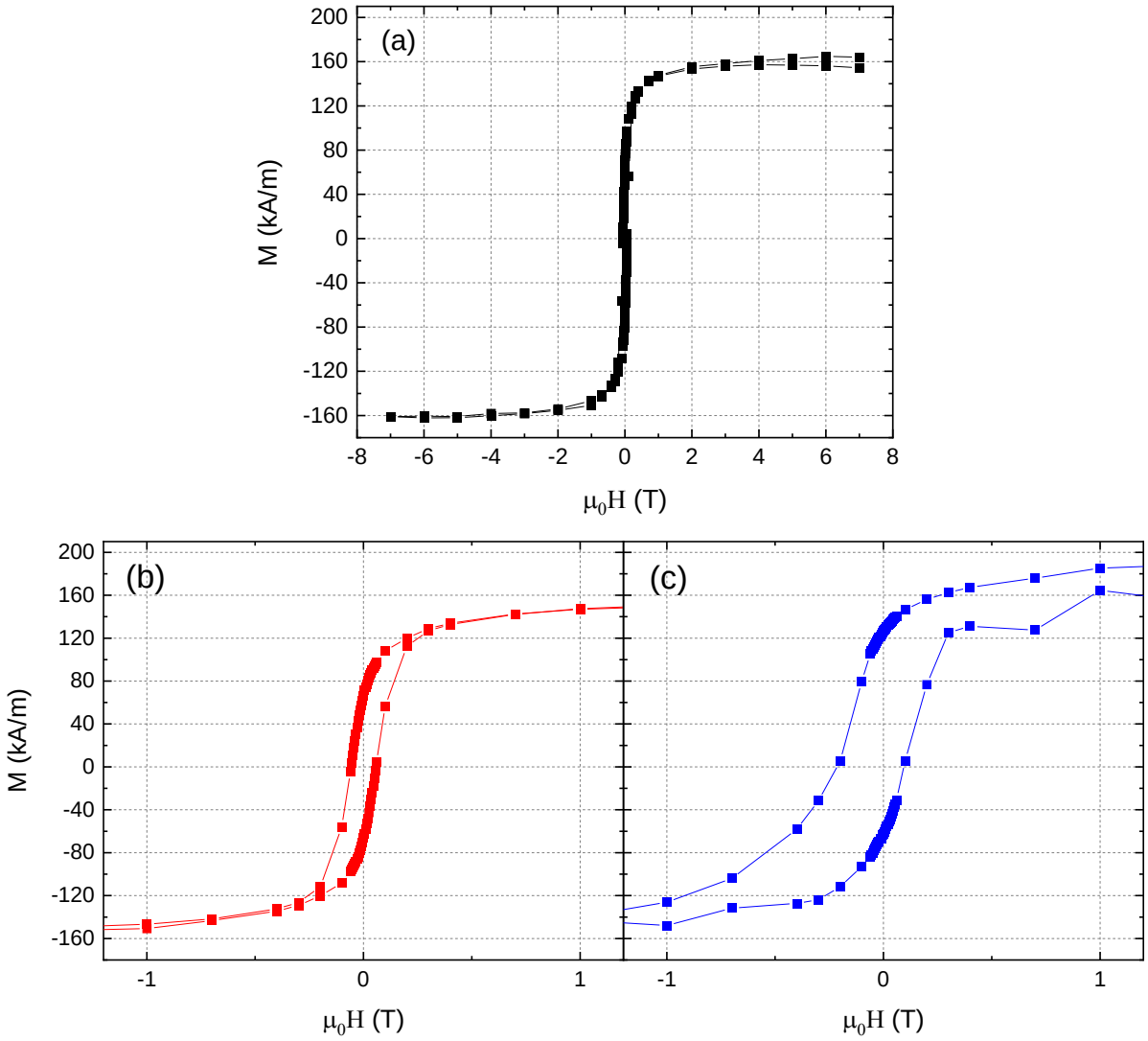

Fig. 4.3: Plots of magnetisation as function of applied field in the plane of thin film grown on sapphire substrate at 300 K in **(a)**, **(b)** and 10 K in **(c)**. H is applied parallel to the <111> direction in the film (i.e. in-plane)

The Fig. 4.3 shows the magnetisation as a function of applied field for the film grown on the sapphire substrate. The measurements were preformed at 300 and 10 K and field was applied in the plane of the film. At 300 K (Fig. 4.3 **(a)**) the saturation magnetisation of the film was found to be 160 kA/m. When compared to other iron oxides the saturation magnetisation is less than Fe_3O_4 (480 kA/m) but more than $\alpha-Fe_2O_3$ (2.5 kA/m) [107]. We see a shift of the hysteresis curve on the field axis as we go to low temperature due to the presence of exchange bias, this points to the co-existence of a mixed ferromagnetic and an antiferromagnetic phase. One possible explanation for the saturation magnetisation can be that one third of the film has Fe_3O_4 phase and rest is antiferromagnetic FeO which does not contribute to the magnetisation, in this scenario we will have 160 kA/m saturation magnetisation.

The magnetisation can also be explained by the canting of the sublattices if we consider a pure antiferromagnetic phase, for instance in case of hematite which contains Fe^{3+} with S = 5/2 and an ion density of $n_{Fe^{3+}}$ = 39.81 nm^{-3}. A canting of 0.31° in hematite produces an magnetisation of 10 kA/m [46]. For FeO film which contains Fe^{2+} with S = 2 and an ion

density of $n_{Fe^{2+}}$ = 50.31 nm^{-3}. A canting angle[1)] of $4.92°$ for the sublattices will result in an saturation magnetisation of 160 kA/m.

4.1.2 On MgO substrate

For the growth of FeO films on MgO(001) substrates the target, laser fluence, repetition rate and temperature were kept the same as in the previous case i.e. $\alpha-Fe_2O_3$, 2.5 J/cm^2, 2 Hz and $390\,°C$, respectively. The reducing formiergas pressure was increased to $65\,\mu bar$. We obtained a thickness of 33 nm with 25,000 pulses and a 3.5 nm thick Pt electrode was deposited ex-situ using DC magnetron sputtering.

The (001)-oriented FeO films were grown on (001)-oriented MgO substrates. MgO has a cubic crystal structure similar to FeO with lattice constant $a = 0.421$ nm. Therefore the lattice mismatch can be calculated using the lattice constants as

$$\epsilon_0 = \frac{a_{FeO} - a_{MgO}}{a_{MgO}} = 2.1\,\% \tag{4.2}$$

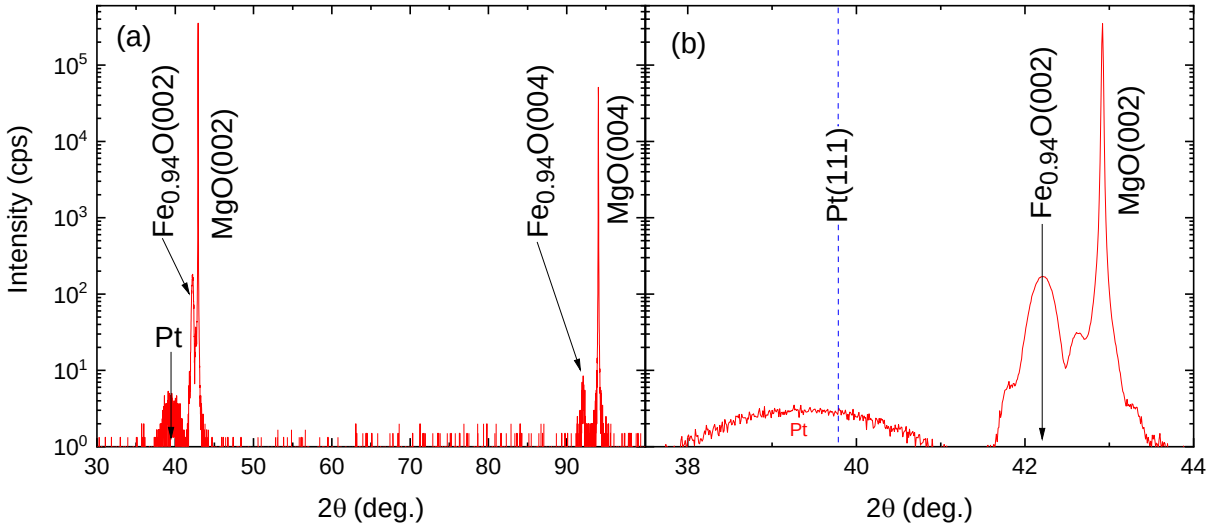

Fig. 4.4: X-ray diffraction diagram. **(a)** and **(b)** show the $2\theta - \omega$ scans of the FeO films on the MgO(001) substrate. Here we see (002) and (004) reflections of the MgO substrate at $2\theta = 42.92°$ and $94.05°$. The (002) and (004) reflections from $Fe_{0.94}O$ are seen at $2\theta = 42.18°$ and $92.03°$. We see the Pt electrode feature around $2\theta = 40°$, the (111) reflection from the bulk Pt is expected at $39.80°$ (dashed blue line in **(b)**). The intensities are given in counts per second.

Similar to the films grown on sapphire substrates we performed X-ray diffraction on the samples on MgO substrates, to characterise the crystallographic structure. The out of plane $2\theta - \omega$ scan only shows reflections which can be attributed either to film or the substrate (Fig. 4.4). We see the expected (00l) reflections from the MgO substrate and the (hkl) reflections (00l) from the FeO film, evidencing that FeO[001] | | MgO[001]. In addition to substrate and FeO reflection we observe a broad feature which can be attributed to the Pt top electrode, since the cubic Pt of lattice constant $a = 0.3920$ nm [106] shows a (111) reflection at $39.80°$. No secondary phases are detected. Using the FeO reflection at θ_{002} =$21.09°$,

[1)] canting angle (α) = $\sin^{-1}(\frac{M}{4n\mu_B})$

θ_{004} =46.01° and via Bragg's law (Eq.(3.1)), we calculated the distance between the FeO {002} planes to $d_{\mathrm{FeO}} = 0.214$ nm. The calculated value of distance between {002} planes is $d_{\mathrm{FeO,literature}} = d_{\mathrm{FeO}}/\sqrt{2^2} = 0.215$ nm, using the literature values of the FeO lattice constant. The lower value of distance between the planes for our sample can be attributed to Fe^{2+} cation vacancies, which reduces the lattice size and hence the inter-planar distance.

For the determination of the layer thickness we apply X-ray reflectometry from $2\theta = 0.5°$ to 5° (Fig. 4.5). The larger oscillations with large period originate from the top Pt electrode and the small oscillations with small period are given by the FeO film. Using the simulation of experimantal data from the LEPTOS software, we obtained a thickness of $t_{\mathrm{FeO}} = 33$ nm and $t_{\mathrm{Pt}} = 3.5$ nm and low (rms) surface roughness of 0.4 nm.

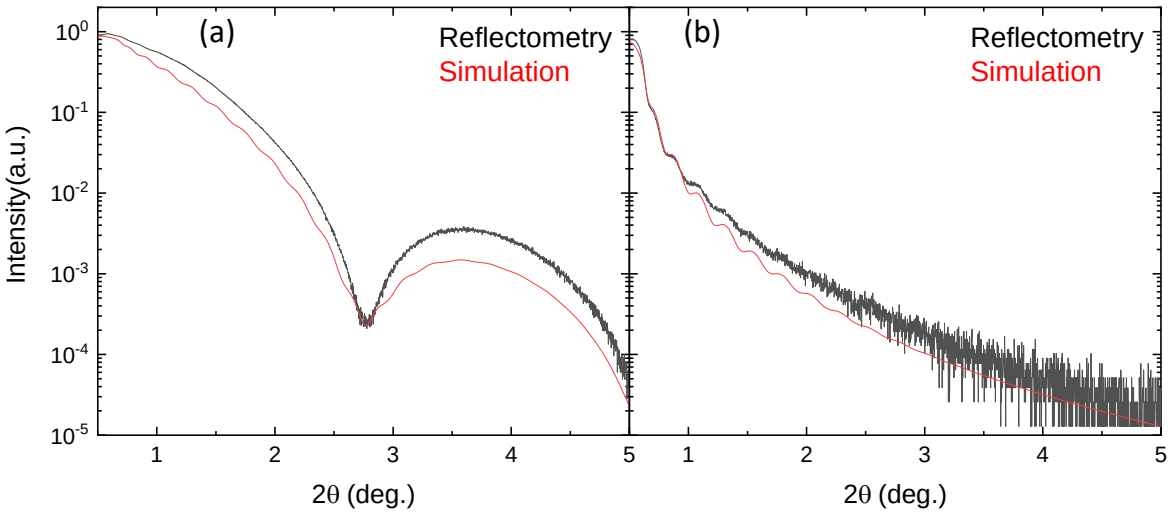

Fig. 4.5: X-ray reflectometry of Pt | FeO(001) bilayer in **(a)** and FeO thin film without Pt layer in **(b)** on MgO substrate. Red curve is the simulated curve on black experimental curve. The simulation is done using the LEPTOS software. The intensity is given in arbitrary units.

4.2 Magnetoresistance (MR) measurements

In order to perform the SMR (c.f. Chap. 2.3) by means of ADMR measurements [7], as shown in Fig. 3.8 the FeO thin films on both the substrates were covered with Pt. Afterwards via optical lithography and Ar ion milling, the samples were pattered into a Hall bar mesa structure (Fig. 3.6). The structure has a width $w = 80\,\mu\mathrm{m}$ and a contact separation of $l_{\mathrm{long}} = 600\,\mu\mathrm{m}$ for the longitudinal and $l_{\mathrm{trans}} = 80\,\mu\mathrm{m}$ for the transverse ADMR measurements (Fig. 3.7). The measurements were performed for field ranging from 1 to 7 T and at three different temperatures 100, 200 and 300 K. All the measurements discussed in this chapter were conducted using the DC current reversal method (c.f. Chap. 3.2.7) with a current of 100 µA being applied to the device. The longitudinal and transverse resistivities (ρ_{long}, ρ_{trans}) for the Hall bar geometry are calculated from the longitudinal and transverse voltages V_{long} and V_{trans} as

$$\rho = \frac{V w t_{\mathrm{Pt}}}{I l} \tag{4.3}$$

Where V is measured with standard four-probe method using a DC current ($I = 100\,\mu\mathrm{A}$) switching method as discussed in Chap. 3.2.7. The Pt layer resistance (ρ_{Pt}) with no exter-

nally applied field and at room temperature is calculated to 2.63 x $10^{-7}\Omega\,\mathrm{m}$ and 2.55 x $10^{-7}\Omega\,\mathrm{m}$ for the case of thin films on sapphire and MgO(001) substrates, respectively. It is in agreement with the literature values of the resistivity of 2.40 x $10^{-7}\Omega\,\mathrm{m}$ [7]. Based on these resistivity measurement we expect the SMR signal to be in the range of $\leq 10^{-4}$. However, the Pt resistivity is temperature (T) dependent (0.4% per K at room temperature [108]) and produces a signal of same order of magnitude if $\Delta T \geq 0.025$ K. This makes these measurement extremely temperature sensitive and challenging to perform.

4.2.1 Angle-dependent Magnetoresistance Measurements in Pt | FeO bilayers

We first study the spin Hall magnetoresistance in Pt | FeO(001) thin films grown on MgO(001) substrates. The measurements were performed at 100, 200 and 300 K by rotating the externally applied magnetic field **H** of a constant magnitude both in (001)-plane of the FeO film as well as out of plane along *j* and *t* directions. During all the measurements the current direction was kept along *j* direction. The measurements were repeated with a magnetic field ranging from 1 to 7 T in steps of 1 T. Figure 4.6 shows a typical set of ADMR measurements, with field rotations along all the three geometries and at three different temperatures of 100, 200 and 300 K. The Pt resistivity ρ_{long} angular dependence

$$\frac{\rho_{(\mathrm{angle})} - \rho_0}{\rho_0} \tag{4.4}$$

is plotted as a function of the magnetic field orientation. Here, ρ_0 represents the constant offset resistivity for angle α, β and γ equal to $90°$ for *ip*, *oopj* and *oopt* rotations, respectively. The *ip* magnetoresistance behaviour as shown in Fig. 4.6 **(a)**, **(d)** and **(g)** for 100, 200 and 300 K, respectively is consistent with the $\cos^2(\alpha)$ dependence. For all the plots in the figure 4.6 we find a characteristic oscillation period of $180°$, but interestingly we observe the oscillations to be similar to ferromagnet not to an antiferromagnet [44–48]. Also, the amplitude increases with increment of applied field for all the three temperatures which is the behaviour observed in antiferromagnets. For *ip* rotations the amplitude reaches a maximum value of 11 x 10^{-4} for measurements done at 7 T and 300 K. Here we need to consider the orientation of the FeO spins in our thin films which is perpendicular to the plane of the film itself. The spins in (111) plane of the FeO point alternatively up and down along the [111] direction, discussed in more detail in Chap. 3.1.3. Now when we apply the magnetic field in the plane of the film this will try to orient the FeO spins towards the field direction itself, this will result in canting of the spins and will produce a net moment in the direction of the field just like ferromagnets.

Therefore, for $\alpha = 0, 180°$ and $360°$, **M** and **s** point perpendicular to each other and hence the spin accumulation at the Pt | FeO(001) interface exerts maximal spin-transfer torque (STT) on the magnetisation of FeO. A finite spin current will flow across the interface and will cause a reduction in the ISHE induced charge current, producing an increase in the voltage, c.f. Chap. 2.3. Similarly, for the lower resistivity cases for $\alpha = 90°$ and $270°$, **M** and **s** are parallelly aligned, hence the spin accumulation cannot exert a STT on the thin film magnetisation, resulting in a small spin current flow through the interface and will produce large ISHE induced charge current and hence a lower voltage. In between the limiting cases the torque is governed by the projection of vector **s** on the magnetisation

M. The slight deviation of the maxima and minima from their theoretical values can be attributed to imperfect alignment of the sample i.e. slightly rotated sample.

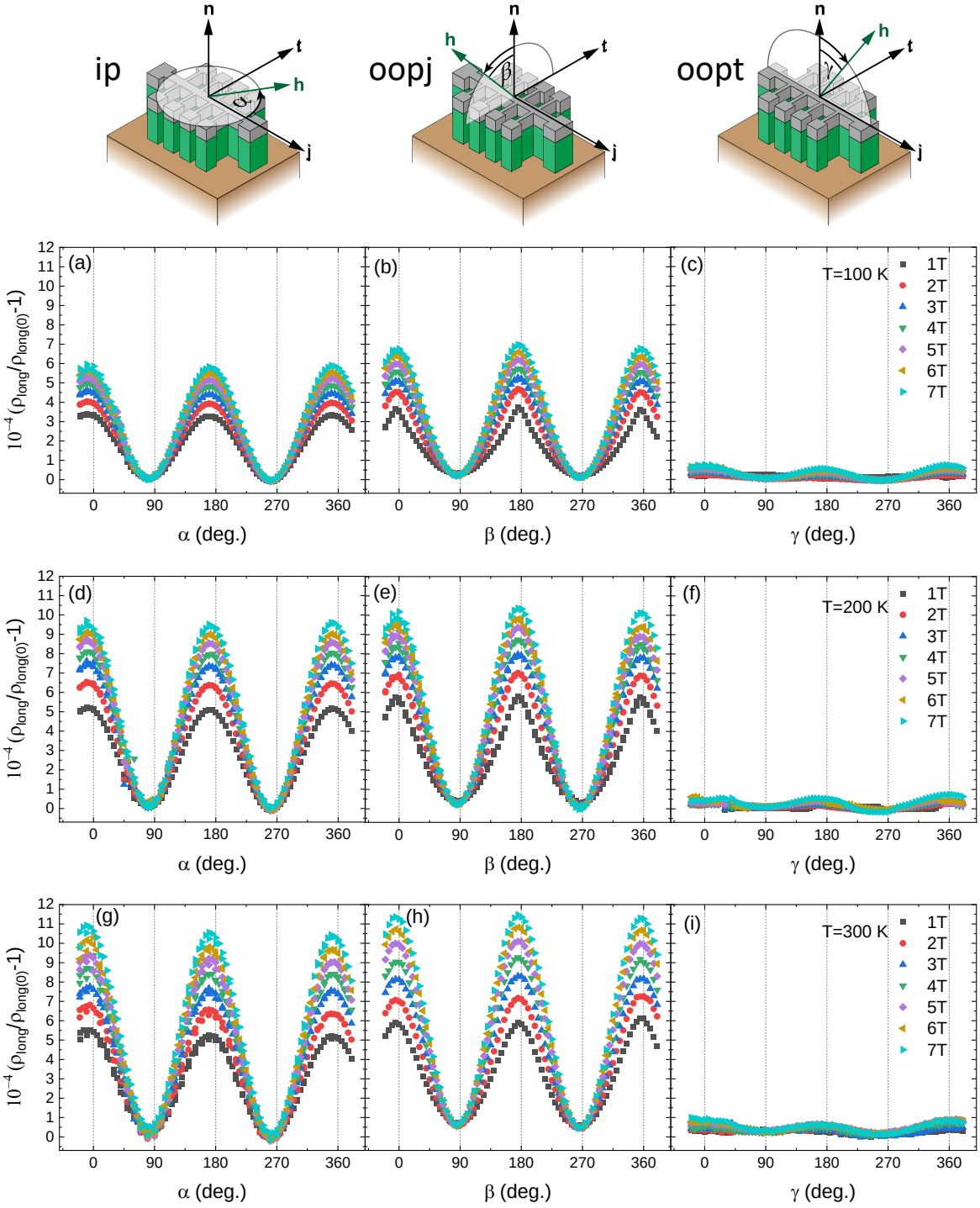

Fig. 4.6: Normalized ADMR measurements of a Pt | FeO(001) bilayer. The upper panels **(a)-(c)** correspond to the measurements done at 100 K, with field ranging from 1 to 7 T in steps on 1 T. Similarly, the middle panels **(d)-(f)** and lower panels **(g)-(i)** correspond to the measurements done at 200 and 300 K, respectively. The first, second and third column correspond to the ip, oopj, oopt measurements, respectively. The rotational geometry is depicted on the top.

The amplitude of the oscillation increases as the applied field increases but it decreases as we decrease the temperature. The decrease in the amplitude with the temperature de-

crease can be attributed to the decrease in the spin Hall angle towards low temperature, i.e. a property of the Pt film [41]. But qualitatively the behaviour remains same for all the three temperatures. The increase in the amplitude with the application of higher field is consistent with the literature and is observed in case of antiferromagnets [44–48]. As with the application of higher field the sublattices will cant more toward the applied field and hence increasing the net magnetisation in the direction of the applied field. This results in a higher magnitude of STT and is reflected as higher SMR amplitude.

Similar trend for the phase and amplitude of the oscillations is seen for the *oopj* field rotations as shown in Fig. 4.6 **(b)**, **(e)** and **(h)**. For *oopj* rotations as well the amplitude increases with the applied field and decreases as the temperature is lowered. For the *oopt* rotations we do not expect the SMR oscillations as the magnetisation (**M**) and spin polarisation (**s**) are always perpendicular to each other. In the Fig. 4.6 **(c)**, **(f)** and **(i)** we observe small oscillations which can be attributed to the anisotropic magnetoresistance. The amplitude increases with higher field application and for a given field the amplitude increases as the temperature is lowered. This behaviour is consistent with the literature [109, 110].

To get a better understanding of ADMR in FeO we performed similar experiments as done earlier, on the thin films grown on sapphire substrates as well. The Fig. 4.7 shows the normalised plots for the measurements performed on Pt | FeO(111) bilayer system grown on Al_2O_3(0001) substrates at 100, 200 and 300 K with fields ranging from 1 to 7 T. All the measurements were performed in the similar setup as done in case of thin films grown on MgO(001) substrates. The in-plane rotations of the applied field are now in the (111) plane of FeO films. The *ip* magnetoresistance behaviour as shown in Fig. 4.7 **(a)**, **(d)** and **(g)** for 100, 200 and 300 K, respectively also follows the characteristic $\cos^2(\alpha)$ dependence. The amplitude increases with the increment of applied field for all the three temperatures. But contrary to what we saw in case of Pt | FeO(001) system here the amplitude is highest for the measurements done at 100 K and decreases as we increase the temperature. As discussed in the Sec. 4.2 the Pt resistivity decreases with decrease in the temperature and hence the SMR signal is expected to decrease for measurements done at low temperatures. The increase in the amplitude with application of higher field can be explained with the canting of the sublattice spins in the direction of the field.

The higher resistive cases for $\alpha = 0, 180^\circ$ and 360°, where **M** and **s** are perpendicular to each other and the low resistive case for $\alpha = \pm 90^\circ$ and 270°, where **M** and **s** are aligned parallelly can be explained with the maximal and minimal STT magnitude at these orientations. Similarly for the intermediate cases torque is governed by the projection of vector **s** on **M**. We also observe an increase in the amplitude of the oscillation with decrease in temperature, this can be explained as an contribution of anisotropic magnetoresistance (AMR) [109, 110].

The *oopj* rotations also show a similar behaviour to *ip* for the phase and amplitude of the oscillations Fig. 4.7 **(b)**, **(e)** and **(h)**. The amplitude increases with the increment of the applied field and for a given field the amplitude further increases as the temperature is lowered. The oscillations observed for the *oopt* rotation Fig. 4.7 **(c)**, **(f)** and **(i)** originate from anisotropic magnetoresistance. The amplitude increases with higher field application and for a given field the amplitude increases as the temperature is lowered this behaviour is consistent with the literature [109, 110].

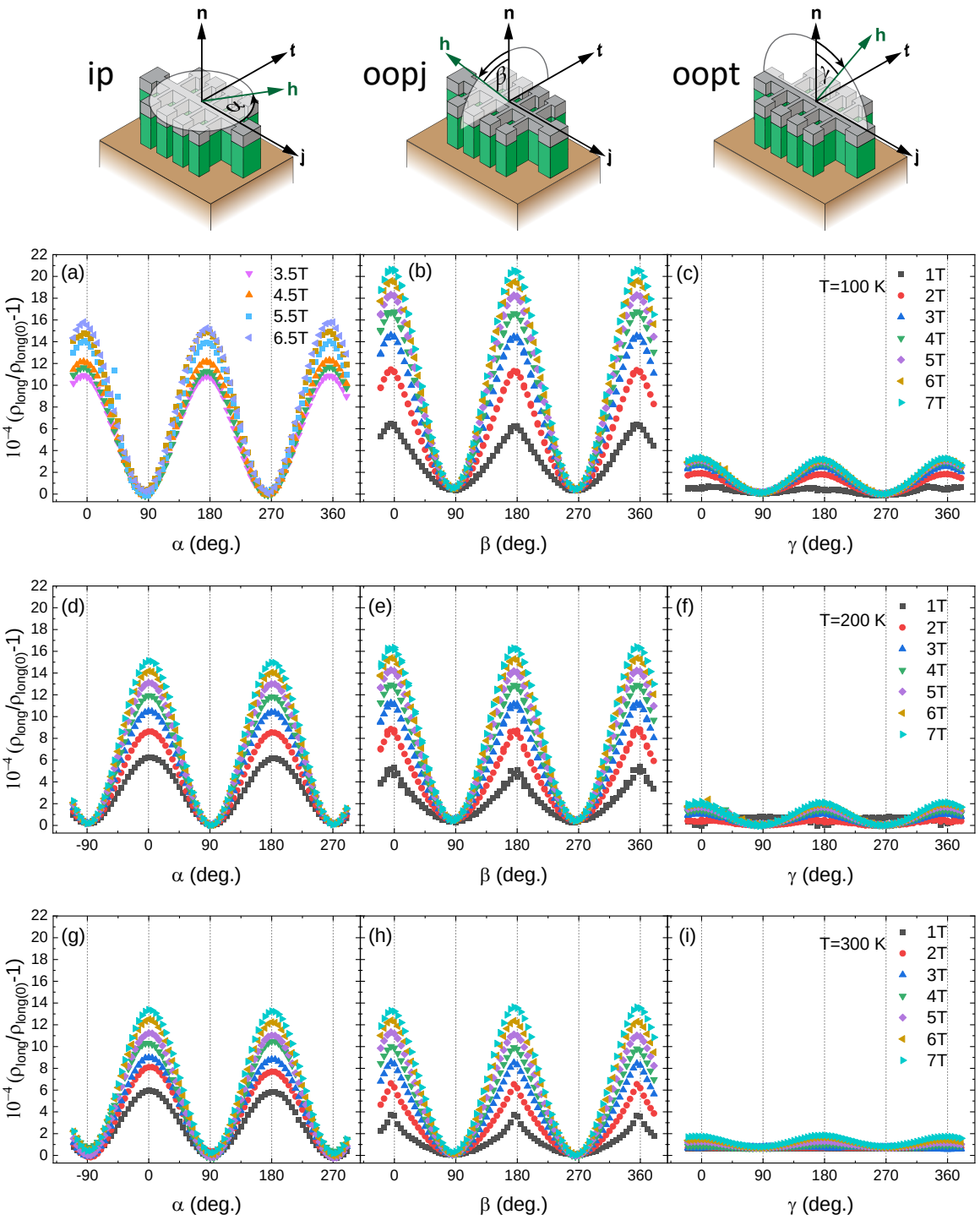

Fig. 4.7: Normalized ADMR measurements of a Pt | FeO(111) bilayer. The upper panels **(a)-(c)** correspond to the measurements done at 100 K, with field ranging from 1 to 7 T in steps on 1 T. Similarly, the middle panels **(d)-(f)** and lower panels **(g)-(i)** correspond to the measurements done at 200 and 300 K, respectively. The first, second and third column correspond to the ip, oopj, oopt measurements, respectively. The rotational geometry is depicted on the top.

4.2.2 Field Dependence

In order to get a better understanding of the field dependence of the SMR amplitude as discussed in Sec. 4.2.1, we extracted the SMR amplitude from the different oscillation plots in the Fig. 4.6 and 4.7. Then we plotted the normalised MR amplitude against different applied field (1-7 T) and at three different temperatures (100, 200 and 300 K) for *ip*, *oopj* and *oopt* rotations (Fig. 4.8, 4.9).

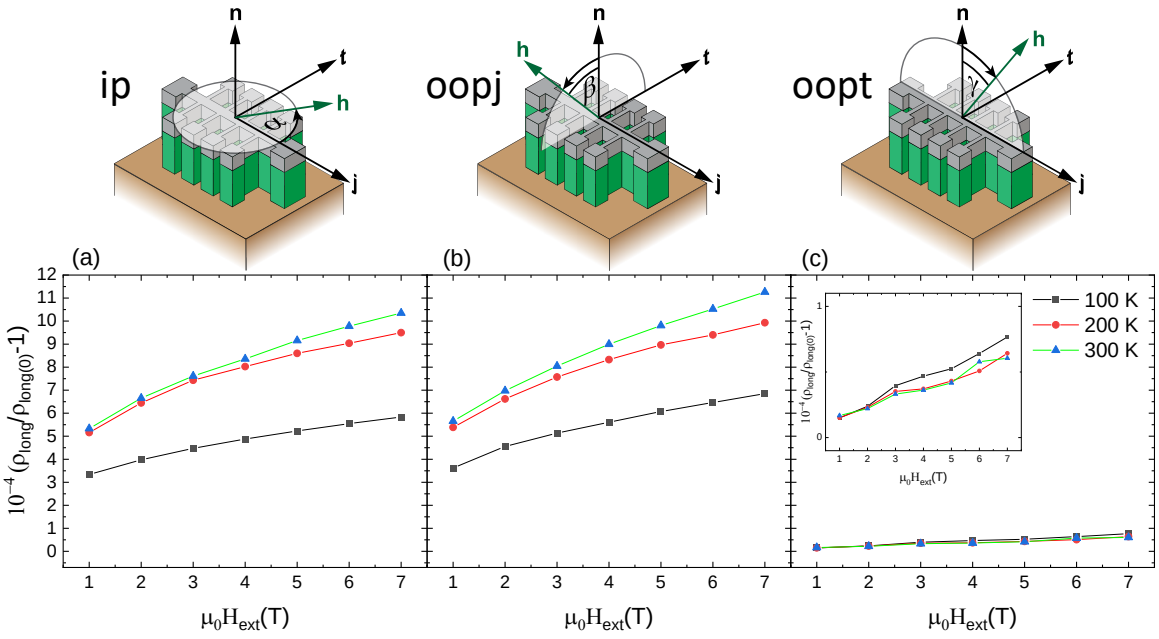

Fig. 4.8: Field dependence of MR in Pt | FeO(001) bilayers for *ip* **(a)**, *oopj* **(b)** and *oopt* **(c)** configurations at 100, 200 and 300 K.

The Fig. 4.8 shows the amplitude vs applied field plots for the Pt | FeO(001) bilayer system. For the *ip* oscillations the amplitude (Fig. 4.8 **(a)**) increases with the increment of the applied field ($\mu_0 H_{\text{ext}}$) and for a given field value the amplitude is larger for higher temperature. The decrease in the amplitude from 300 to 200 K is relatively smaller when compare to the decrease from 200 to 100 K. The 7 T field is not enough to saturate our system as we still see a slope if we go at higher fields.

For the *oopj* oscillations the amplitude (Fig. 4.8 **(b)**) behaviour is similar to the *ip*, but for a given field value the amplitude is higher than the *ip*, as in *oopj* we see a contribution from the *oopt* oscillations as well. For *oopt* oscillations (Fig. 4.8 **(c)**) the lowest temperature has the highest amplitude as these oscillations arise from the anisotropic magnetoresistance which increases with decrease in the temperature [109, 110]. We observe similar field dependence here as well, the amplitude increases as the applied field is increased.

We also prepared similar plots for the Pt | FeO(111) thin films grown on sapphire substrates as shown in Fig. 4.9. Here we immediately observe the amplitude is highest for the lowest temperature for all the three geometries. Firstly we discuss the *ip* rotations (Fig. 4.9 **(a)**), where the amplitude increases as the applied field increases, here as well the 7 T field is not enough to saturate the amplitude. For a given field value the amplitude is highest for low temperatures. Similar trend is seen for *oopj* orientation (Fig. 4.9 **(b)**), but the amplitude is higher than the *ip* case as here the amplitude has contributions from the *oopt* rotations

as well. The *oopt* amplitude (Fig. 4.9 **(c)**) also increases with the applied field and shows a similar temperature dependence. The amplitude also shows signs of saturation as we go towards the higher fields.

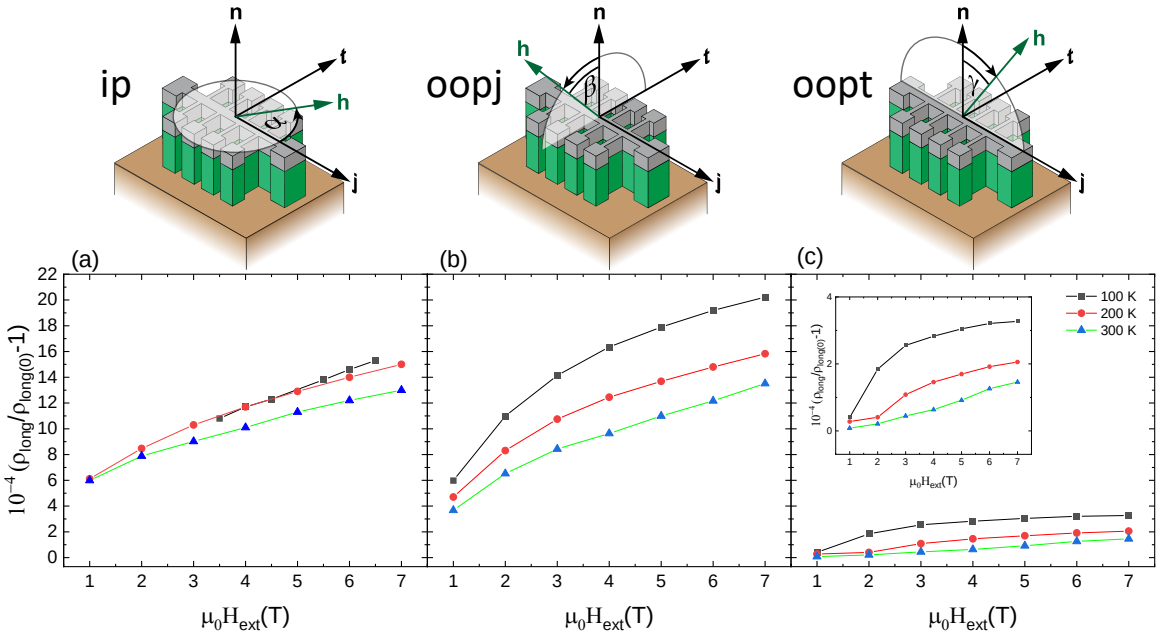

Fig. 4.9: Field dependence of MR in Pt | FeO(111) bilayers for *ip* **(a)**, *oopj* **(b)** and *oopt* **(c)** configurations at 100, 200 and 300 K.

4.3 Summary

In this chapter we discussed the spin Hall magnetoresistance (SMR) in normal metal Pt and antiferromagnetically insulating FeO heterostructures, grown in two different orientations i.e. (111) oriented on Al_2O_3(0001) and (001) oriented on MgO(001) substrates. The main focus of this study was to understand the amplitude of SMR relative to the existing literature value and see its dependence with the spin density of the system.

To study this we conducted SMR measurements in three orthogonal planes at three different temperatures i.e. 100, 200 and 300 K, with field varying from 1 to 7 T (c.f. Chap. 4.2.1). The SMR oscillations were observed in both the cases i.e. films on MgO and sapphire substrates but the oscillations phase was similar to ferromagnets not to the antiferromagnets as we expected. Interestingly, the amplitude in case films on sapphire increased at we went to lower temperatures.

Additionally, we also observed a field and temperature dependence of the SMR amplitude (c.f. Chap. 4.2.2). The amplitude increases as we increased the applied field. For a given field value in the *ip* and *oopj* configuration the amplitude was highest for higher temperature in the films on MgO. But the situation was opposite in case of films on sapphire where for *ip* and *oopj* conigurations the amplitude was highest for the low temperatures. For *oopt* rotations the amplitude was highest for the low temperature for both the films.

5 Summary and Outlook

In this thesis, we investigated spin transport in bilayer heterostructures consisting of normal metal Pt and antiferromagnetic insulator FeO. Applying a dc charge current $\boldsymbol{j}_c$ through the Pt strip will result in a transverse spin current $\boldsymbol{j}_s$ via spin Hall effect (SHE) and will produce an electron spin accumulation with polarisation $\boldsymbol{s} \perp \boldsymbol{j}_c$ at the Pt | AFI interface. The spin polarisation interacts with the sublattice magnetisation of the antiferromagnetic insulator layer and leads to the observable characteristic oscillation in the resistivity by the virtue of spin Hall magnetoresistance (SMR). Here we will present a short summary of the key findings of this work, followed by some proposals for the future experiments in Sec. 5.2.

5.1 Summary

In Chapter 4, we studied the spin Hall magnetoresistance (SMR) effect in Pt | FeO bilayer systems grown along (111) and (001) orientation on Al_2O_3 and MgO(001) substrates, respectively. The samples were covered with Pt top electrode and were patterned into Hall bar mesa structure via optical lithography and Ar ion milling. We studied the magnetoresistance by rotating the magnetic field of constant magnitude ranging from 1 to 7 T both in and out of the plane geometries at 100, 200 and 300 K. For *ip*, *oopj* and *oopt* we observed the characteristic SMR periodic oscillations of $180°$ for longitudinal resistance for films on both the substrates. Interestingly, we saw the SMR oscillations at room temperature which is well above the magnetic ordering Neel temperature of 198 K for FeO.

The phase was found to be similar to a ferrimagnet and was not shifted by $90°$ as reported for other antiferromagnetic systems like Pt | NiO and Pt | $\alpha-Fe_2O_3$ [46, 47]. The maximum normalised *ip* SMR amplitude for the films on sapphire was found to be 16 x 10^{-4} at 100K and 6.5 T. Whereas for the films on MgO(001) it was 11 x 10^{-4} at 300K and 7 T. Both of these values are higher than NiO but lower than hematite. Fot *oopj* rotations the maximum amplitude for films on sapphire was 20 x 10^{-4} at 100 K and 7 T. For films on MgO(001) it was 12 x 10^{-4} at 300 K and 7 T. This increase in the amplitude was attributed to the AMR contributions. The *oopt* rotations showed oscillations with small oscillations mainly arising from the AMR.

5.2 Outlook

In this section we offer a short outlook to the possible future investigations of the FeO films studied in this work. In this work we studied the FeO films grown along (111) and (001) orientations. Since the FeO spins point perpendicular to the (111) plane along the [111] direction, it will be beneficial to study the SMR in (110) oriented FeO films. Then, two of the four {111} directions, i.e. (-111) and (1-11), will be in the sample plane. It will provide a comprehensive idea about how the sublattice magnetisation behaves. In our study we found that the amplitude was not saturated till maximum field of 7 T hence, it will be useful to see the amplitude evolution with fields above 7 T. Similarly, temperature and field sweeps will provide a better picture of the system's dependence on these parameters. One would also like to investigate the transverse voltage signal and then compare the determined SMR

amplitude with the current data of SMR amplitude that we have from the longitudinal signal.

A Appendix: PLD FeO Films

In this Section we summarize the FeO samples grown using PLD at the Walther-Meißner-Institut with the corresponding growth parameters.

ID	$T_{\mathrm{sample}}(^{\circ}\mathrm{C})$	number of laser pulses	Growth atmosphere	Pressure (µbar)	Substrate
FMS1	600	20000	Ar	25	Al_2O_3(0001)
FMS9	700	6000	Ar	25	Al_2O_3(0001)
FMS18	650	10000	N_2/H_2	25	MgO(111)
FMS21	650	6000	N_2/H_2	25	MgO(001)
FMS30	650	6000	N_2/H_2	35	MgO(001)
FMS31	650	6000	N_2/H_2	45	MgO(001)
FMS32	650	6000	N_2/H_2	55	MgO(001)
FMS54	390	20000	Ar/H_2	35	Al_2O_3(0001)
FMS55	390	20000	Ar/H_2	35	MgO(001)
FMS56	390	25000	Ar/H_2	55	Al_2O_3(0001)
FMS57	390	25000	Ar/H_2	55	MgO(001)
FMS58	390	25000	Ar/H_2	40	Al_2O_3(0001)
FMS59	390	25000	Ar/H_2	65	MgO(001)
FMS60	390	25000	Ar/H_2	30	Al_2O_3(0001)
FMS61	390	25000	Ar/H_2	65	MgO(001)
FMS64	390	25000	Ar/H_2	25	Al_2O_3(0001)
FMS69	390	10000	Ar/H_2	25	Al_2O_3(0001)

Tab. A.1: List of some of the PLD-grown FeO samples prepared during this work with indicated sample growth temperature T_{sample}, number of laser pulses, growth atmosphere (N_2/H_2 and Ar/H_2 represents the formiergas with composition 95%/5%), chamber pressure during the growth process and substrate used. The laser is a pulsed UV-excimer laser (KrF, $248\,\mathrm{nm}$) and the energy density per pulse was $2.5\,\mathrm{Jcm}^{-2}$.

References

[1] X. Lin, W. Yang, K. L. Wang & W. Zhao. Two-dimensional spintronics for low-power electronics (2019).

[2] F. Pulizzi. The rise of semiconductor spintronics. *Nature Physics* **4**, S20–S20 (2008). URL.

[3] O. Smith. Oberlin Smith and the Invention of Magnetic Sound Recording An Appreciation on the 150th Anniversary of the Inventor's Birth (1888).

[4] M. N. Baibich, J. M. Broto, A. Fert, F. N. Van Dau, F. Petroff, P. Eitenne, G. Creuzet, A. Friederich & J. Chazelas. Giant magnetoresistance of (001)Fe/(001)Cr magnetic superlattices. *Physical Review Letters* **61**, 2472–2475 (1988). URL.

[5] G. Binasch, P. Grünberg, F. Saurenbach & W. Zinn. Enhanced magnetoresistance in layered magnetic structures with antiferromagnetic interlayer exchange. *Physical Review B* **39**, 4828–4830 (1989). URL.

[6] H. Nakayama, M. Althammer, Y. T. Chen, K. Uchida, Y. Kajiwara, D. Kikuchi, T. Ohtani, S. Geprägs, M. Opel, S. Takahashi, R. Gross, G. E. Bauer, S. T. Goennenwein & E. Saitoh. Spin Hall Magnetoresistance Induced by a Nonequilibrium Proximity Effect. *Physical Review Letters* **110**, 206601 (2013). URL.

[7] M. Althammer, S. Meyer, H. Nakayama, M. Schreier, S. Altmannshofer, M. Weiler, H. Huebl, S. Geprägs, M. Opel, R. Gross, D. Meier, C. Klewe, T. Kuschel, J. M. Schmalhorst, G. Reiss, L. Shen, A. Gupta, Y. T. Chen, G. E. Bauer, E. Saitoh & S. T. Goennenwein. Quantitative study of the spin Hall magnetoresistance in ferromagnetic insulator/normal metal hybrids. *Physical Review B - Condensed Matter and Materials Physics* **87**, 224401 (2013), 1304.6151. URL.

[8] Y. T. Chen, S. Takahashi, H. Nakayama, M. Althammer, S. T. Goennenwein, E. Saitoh & G. E. Bauer. Theory of spin Hall magnetoresistance. *Physical Review B - Condensed Matter and Materials Physics* **87**, 144411 (2013). URL.

[9] A. B. Shick, S. Khmelevskyi, O. N. Mryasov, J. Wunderlich & T. Jungwirth. Spin-orbit coupling induced anisotropy effects in bimetallic antiferromagnets: A route towards antiferromagnetic spintronics. *Physical Review B - Condensed Matter and Materials Physics* **81**, 212409 (2010), 1002.2151. URL.

[10] A. S. Núñez, R. A. Duine, P. Haney & A. H. MacDonald. Theory of spin torques and giant magnetoresistance in antiferromagnetic metals. *Physical Review B - Condensed Matter and Materials Physics* **73**, 214426 (2006). URL.

[11] A. H. MacDonald & M. Tsoi. Antiferromagnetic metal spintronics. 0510797 (2011).

[12] V. M. Barthem, C. V. Colin, H. Mayaffre, M. H. Julien & D. Givord. Revealing the properties of Mn 2 Au for antiferromagnetic spintronics. *Nature Communications* **4**, 2892–2892 (2013). URL.

[13] E. V. Gomonay & V. M. Loktev. Spintronics of antiferromagnetic systems (2014).

[14] R. Macêdo & T. Dumelow. Tunable all-angle negative refraction using antiferromagnets. *Physical Review B - Condensed Matter and Materials Physics* **89**, 035135 (2014). URL.

[15] J. Železný, H. Gao, K. Výborný, J. Zemen, J. Mašek, A. Manchon, J. Wunderlich, J. Sinova & T. Jungwirth. Relativistic néel-order fields induced by electrical current in antiferromagnets. *Physical Review Letters* **113**, 157201 (2014), 1410.8296. URL.

[16] R. Cheng, J. Xiao, Q. Niu & A. Brataas. Spin pumping and spin-transfer torques in antiferromagnets. *Physical Review Letters* **113**, 057601 (2014), 1404.4023. URL.

[17] V. Tshitoyan, C. Ciccarelli, A. P. Mihai, M. Ali, A. C. Irvine, T. A. Moore, T. Jungwirth & A. J. Ferguson. Electrical manipulation of ferromagnetic NiFe by antiferromagnetic IrMn. *Physical Review B - Condensed Matter and Materials Physics* **92**, 214406 (2015). URL.

[18] T. Jungwirth, X. Marti, P. Wadley & J. Wunderlich. Antiferromagnetic spintronics. 1509.05296 (2016).

[19] T. Satoh, R. Iida, T. Higuchi, M. Fiebig & T. Shimura. Writing and reading of an arbitrary optical polarization state in an antiferromagnet. *Nature Photonics* **9**, 25–29 (2014). URL.

[20] X. Marti, I. Fina, C. Frontera, J. Liu, P. Wadley, Q. He, R. J. Paull, J. D. Clarkson, J. Kudrnovský, I. Turek, J. Kuneš, D. Yi, J. H. Chu, C. T. Nelson, L. You, E. Arenholz, S. Salahuddin, J. Fontcuberta, T. Jungwirth & R. Ramesh. Room-temperature antiferromagnetic memory resistor. *Nature Materials* **13**, 367–374 (2014). URL.

[21] P. Wadley, B. Howells, J. Železný, C. Andrews, V. Hills, R. P. Campion, V. Novák, K. Olejník, F. Maccherozzi, S. S. Dhesi, S. Y. Martin, T. Wagner, J. Wunderlich, F. Freimuth, Y. Mokrousov, J. Kuneš, J. S. Chauhan, M. J. Grzybowski, A. W. Rushforth, K. Edmond, B. L. Gallagher & T. Jungwirth. Spintronics: Electrical switching of an antiferromagnet. *Science* **351**, 587–590 (2016). URL.

[22] H. Chen, Q. Niu & A. H. Macdonald. Anomalous hall effect arising from noncollinear antiferromagnetism. *Physical Review Letters* **112**, 017205 (2014). URL.

[23] J. B. Mendes, R. O. Cunha, O. Alves Santos, P. R. Ribeiro, F. L. Machado, R. L. Rodríguez-Suárez, A. Azevedo & S. M. Rezende. Large inverse spin Hall effect in the antiferromagnetic metal Ir20 Mn80. *Physical Review B - Condensed Matter and Materials Physics* **89**, 140406 (2014). URL.

[24] W. Zhang, M. B. Jungfleisch, W. Jiang, J. E. Pearson, A. Hoffmann, F. Freimuth & Y. Mokrousov. Spin hall effects in metallic antiferromagnets. *Physical Review Letters* **113**, 196602 (2014). URL.

[25] Y. Ou, S. Shi, D. C. Ralph & R. A. Buhrman. Strong spin Hall effect in the antiferromagnet PtMn. *Physical Review B* **93**, 220405 (2016), 1603.08068. URL.

[26] Y. Ohnuma, H. Adachi, E. Saitoh & S. Maekawa. Spin Seebeck effect in antiferromagnets and compensated ferrimagnets. *Physical Review B - Condensed Matter and Materials Physics* **87**, 014423 (2013), 1211.0123. URL.

[27] S. Seki, T. Ideue, M. Kubota, Y. Kozuka, R. Takagi, M. Nakamura, Y. Kaneko, M. Kawasaki & Y. Tokura. Thermal Generation of Spin Current in an Antiferromagnet. *Physical Review Letters* **115**, 266601 (2015), 1508.02555. URL.

[28] S. M. Wu, W. Zhang, A. Kc, P. Borisov, J. E. Pearson, J. S. Jiang, D. Lederman, A. Hoffmann & A. Bhattacharya. Antiferromagnetic Spin Seebeck Effect. *Physical Review Letters* **116**, 097204 (2016), 1509.00439. URL.

[29] S. M. Rezende, R. L. Rodríguez-Suárez & A. Azevedo. Theory of the spin Seebeck effect in antiferromagnets. *Physical Review B* **93**, 014425 (2016). URL.

[30] P. Merodio, A. Ghosh, C. Lemonias, E. Gautier, U. Ebels, M. Chshiev, H. Béa, V. Baltz & W. E. Bailey. Penetration depth and absorption mechanisms of spin currents in Ir 20Mn80 and Fe50Mn50 polycrystalline films by ferromagnetic resonance and spin pumping. *Applied Physics Letters* **104**, 103913 (2014). URL.

[31] H. Wang, C. Du, P. C. Hammel & F. Yang. Antiferromagnonic spin transport from Y3Fe5 O12 into NiO. *Physical Review Letters* **113**, 097202 (2014). URL.

[32] C. Hahn, G. De Loubens, V. V. Naletov, J. Ben Youssef, O. Klein & M. Viret. Conduction of spin currents through insulating antiferromagnetic oxides. *EPL* **108**, 57005 (2014). URL.

[33] H. Wang, C. Du, P. C. Hammel & F. Yang. Spin transport in antiferromagnetic insulators mediated by magnetic correlations. *Physical Review B - Condensed Matter and Materials Physics* **91**, 220410 (2015). URL.

[34] T. Moriyama, S. Takei, M. Nagata, Y. Yoshimura, N. Matsuzaki, T. Terashima, Y. Tserkovnyak & T. Ono. Anti-damping spin transfer torque through epitaxial nickel oxide. *Applied Physics Letters* **106**, 103913 (2015). URL.

[35] W. Lin, K. Chen, S. Zhang & C. L. Chien. Enhancement of Thermally Injected Spin Current through an Antiferromagnetic Insulator. *Physical Review Letters* **116**, 186601 (2016), 1603.00931. URL.

[36] T. Shang, Q. F. Zhan, H. L. Yang, Z. H. Zuo, Y. L. Xie, L. P. Liu, S. L. Zhang, Y. Zhang, H. H. Li, B. M. Wang, Y. H. Wu, S. Zhang & R. W. Li. Effect of NiO inserted layer on spin-Hall magnetoresistance in Pt/NiO/YIG heterostructures. *Applied Physics Letters* **109**, 32410 (2016). URL.

[37] J. E. Hirsch. Spin hall effect. *Physical Review Letters* **83**, 1834–1837 (1999), 9906160. URL.

[38] N. Vlietstra, J. Shan, V. Castel, B. J. Van Wees & J. Ben Youssef. Spin-Hall magnetoresistance in platinum on yttrium iron garnet: Dependence on platinum thickness

and in-plane/out-of-plane magnetization. *Physical Review B - Condensed Matter and Materials Physics* **87**, 184421 (2013), 1301.3266. URL.

[39] C. Hahn, G. De Loubens, O. Klein, M. Viret, V. V. Naletov & J. Ben Youssef. Comparative measurements of inverse spin Hall effects and magnetoresistance in YIG/Pt and YIG/Ta. *Physical Review B - Condensed Matter and Materials Physics* **87**, 174417 (2013), 1302.4416. URL.

[40] S. R. Marmion, M. Ali, M. McLaren, D. A. Williams & B. J. Hickey. Temperature dependence of spin Hall magnetoresistance in thin YIG/Pt films. *Physical Review B - Condensed Matter and Materials Physics* **89**, 220404 (2014). URL.

[41] S. Meyer, M. Althammer, S. Geprägs, M. Opel, R. Gross & S. T. Goennenwein. Temperature dependent spin transport properties of platinum inferred from spin Hall magnetoresistance measurements. *Applied Physics Letters* **104**, 242411 (2014), 1401.7787. URL.

[42] M. Aldosary, J. Li, C. Tang, Y. Xu, J. G. Zheng, K. N. Bozhilov & J. Shi. Platinum/yttrium iron garnet inverted structures for spin current transport. *Applied Physics Letters* **108**, 242401 (2016). URL.

[43] M. Isasa, A. Bedoya-Pinto, S. Vélez, F. Golmar, F. Sánchez, L. E. Hueso, J. Fontcuberta & F. Casanova. Spin Hall magnetoresistance at Pt/CoFe2O4 interfaces and texture effects. *Applied Physics Letters* **105**, 142402 (2014), 1307.1267. URL.

[44] S. Geprägs, M. Opel, J. Fischer, O. Gomonay, P. Schwenke, M. Althammer, H. Huebl & R. Gross. Spin Hall magnetoresistance in antiferromagnetic insulators. *Journal of Applied Physics* **127**, 243902 (2020), 2004.02639. URL.

[45] A. A. B. Lidiard -Ferrites, A. Fairweather, F. F. Roberts & A. J. E. Welch. Antiferromagnetism and Ferrimagnetism Related content. Tech. Rep.

[46] J. Fischer, M. Althammer, N. Vlietstra, H. Huebl, S. T. Goennenwein, R. Gross, S. Geprägs & M. Opel. Large Spin Hall Magnetoresistance in Antiferromagnetic α-Fe2 O3/Pt Heterostructures. *Physical Review Applied* **13**, 014019 (2020), 1907.13393. URL.

[47] J. Fischer, O. Gomonay, R. Schlitz, K. Ganzhorn, N. Vlietstra, M. Althammer, H. Huebl, M. Opel, R. Gross, S. T. Goennenwein & S. Geprägs. Spin Hall magnetoresistance in antiferromagnet/heavy-metal heterostructures. *Physical Review B* **97**, 014417 (2018), 1709.04158. URL.

[48] A. N. Bogdanov, A. V. Zhuravlev & U. K. Rößler. Spin-flop transition in uniaxial antiferromagnets: Magnetic phases, reorientation effects, and multidomain states. *Physical Review B - Condensed Matter and Materials Physics* **75**, 094425 (2007), 0609648. URL.

[49] Y. M. Hung, C. Hahn, H. Chang, M. Wu, H. Ohldag & A. D. Kent. Spin transport in antiferromagnetic NiO and magnetoresistance in Y3Fe5O12/NiO/Pt structures. *AIP Advances* **7**, 55903 (2017). URL.

[50] W. Lin & C. L. Chien. Electrical Detection of Spin Backflow from an Antiferromagnetic Insulator/ Y3Fe5 O12 Interface. *Physical Review Letters* **118**, 067202 (2017). URL.

[51] A. Aqeel, N. Vlietstra, A. Roy, M. Mostovoy, B. J. Van Wees & T. T. Palstra. Electrical detection of spiral spin structures in Pt | Cu2OSeO3 heterostructures. *Physical Review B* **94**, 134418 (2016), 1607.05630. URL.

[52] K. Ganzhorn, J. Barker, R. Schlitz, B. A. Piot, K. Ollefs, F. Guillou, F. Wilhelm, A. Rogalev, M. Opel, M. Althammer, S. Geprägs, H. Huebl, R. Gross, G. E. Bauer & S. T. Goennenwein. Spin Hall magnetoresistance in a canted ferrimagnet. *Physical Review B* **94**, 094401 (2016), 1605.07441. URL.

[53] N. F. M. Ott & H. H. Wills. The electrical conductivity of transition metals. *Proceedings of the Royal Society of London. Series A - Mathematical and Physical Sciences* **153**, 699–717 (1936). URL.

[54] T. Wimmer. *Spin transport in magnetic nanostructutes*. Masters thesis, Technische Universität München (2016).

[55] J. Shi, P. Zhang, D. Xiao & Q. Niu. Proper definition of spin current in spin-orbit coupled systems. *Physical Review Letters* **96**, 076604 (2006). URL.

[56] P. Q. Jin, Y. Q. Li & F. C. Zhang. SU(2) × U(1) unified theory for charge, orbit and spin currents. *Journal of Physics A: Mathematical and General* **39**, 7115–7123 (2006), 0502231. URL.

[57] A. Vernes, B. L. Györffy & P. Weinberger. Spin currents, spin-transfer torque, and spin-Hall effects in relativistic quantum mechanics. *Physical Review B - Condensed Matter and Materials Physics* **76**, 012408 (2007). URL.

[58] S. Lowitzer, D. Ködderitzsch & H. Ebert. Spin projection and spin current density within relativistic electronic-transport calculations. *Physical Review B - Condensed Matter and Materials Physics* **82**, 140402 (2010). URL.

[59] M. I. D'Yakonov, V. I. Perel', M. I. D'Yakonov & V. I. Perel'. Possibility of Orienting Electron Spins with Current. *JETPL* **13**, 467 (1971). URL.

[60] Y. K. Kato, R. C. Myers, A. C. Gossard & D. D. Awschalom. Observation of the spin hall effect in semiconductors. *Science* **306**, 1910–1913 (2004). URL.

[61] J. Smit. The spontaneous hall effect in ferromagnetics II. *Physica* **24**, 39–51 (1958).

[62] M. Julliere. Tunneling between ferromagnetic films. *Physics Letters A* **54**, 225–226 (1975).

[63] L. Berger. Side-jump mechanism for the hall effect of ferromagnets. *Physical Review B* **2**, 4559–4566 (1970). URL.

[64] D. Xiao, M. C. Chang & Q. Niu. Berry phase effects on electronic properties. *Reviews of Modern Physics* **82**, 1959–2007 (2010), 0907.2021. URL.

[65] P. Jacquod, R. S. Whitney, J. Meair & M. Büttiker. Onsager relations in coupled electric, thermoelectric, and spin transport: The tenfold way. *Physical Review B - Condensed Matter and Materials Physics* **86**, 155118 (2012), 1207.1629. URL.

[66] T. Wimmer. *Controlling magnonic spin currents in magnetic insulators*. Phd thesis, Technische Universität München (2021).

[67] M. Schreier, G. E. Bauer, V. I. Vasyuchka, J. Flipse, K. I. Uchida, J. Lotze, V. Lauer, A. V. Chumak, A. A. Serga, S. Daimon, T. Kikkawa, E. Saitoh, B. J. Van Wees, B. Hillebrands, R. Gross & S. T. Goennenwein. Sign of inverse spin Hall voltages generated by ferromagnetic resonance and temperature gradients in yttrium iron garnet platinum bilayers. *Journal of Physics D: Applied Physics* **48**, 025001 (2015), 1404.3490. URL.

[68] S. O. Valenzuela & M. Tinkham. Direct electronic measurement of the spin Hall effect. *Nature* **442**, 176–179 (2006), 0605423. URL.

[69] L. Liu, C. F. Pai, Y. Li, H. W. Tseng, D. C. Ralph & R. A. Buhrman. Spin-torque switching with the giant spin hall effect of tantalum. *Science* **336**, 555–558 (2012), 1203.2875. URL.

[70] E. Saitoh, M. Ueda, H. Miyajima & G. Tatara. Conversion of spin current into charge current at room temperature: Inverse spin-Hall effect. *Applied Physics Letters* **88**, 182509 (2006). URL.

[71] K. Uchida, S. Takahashi, K. Harii, J. Ieda, W. Koshibae, K. Ando, S. Maekawa & E. Saitoh. Observation of the spin Seebeck effect. *Nature* **455**, 778–781 (2008). URL.

[72] C. Chen, D. Tian, H. Zhou, D. Hou & X. Jin. Generation and Detection of Pure Spin Current in an H -Shaped Structure of a Single Metal. *Physical Review Letters* **122**, 016804 (2019). URL.

[73] Kelvin. XIX. On the electro-dynamic qualities of metals:—Effects of magnetization on the electric conductivity of nickel and of iron. *Proceedings of the Royal Society of London* **8**, 546–550 (1857). URL.

[74] T. R. Mcguire & R. I. Potter. Anisotropic Magnetoresistance in Ferromagnetic 3D Alloys. *IEEE Transactions on Magnetics* **11**, 1018–1038 (1975).

[75] F. Maximilian. Bachelorthesis Abschlussarbeit im Bachelorstudiengang Physik Fabrication and Characterization of Y 3 Fe 5 O 12 | Pt | Y 3 Fe 5 O 12 Trilayers for Spin Current Based Experiments Herstellung und Charakterisierung von Y 3 Fe 5 O 12 | Pt | Y 3 Fe 5 O 12 Trilagen fü. Tech. Rep. (2013).

[76] A. Manchon, J. Železný, I. M. Miron, T. Jungwirth, J. Sinova, A. Thiaville, K. Garello & P. Gambardella. Current-induced spin-orbit torques in ferromagnetic and antiferromagnetic systems. *Reviews of Modern Physics* **91**, 035004 (2019), 1801.09636. URL.

[77] M. Johnson & R. H. Silsbee. Interfacial charge-spin coupling: Injection and detection of spin magnetization in metals. *Physical Review Letters* **55**, 1790–1793 (1985). URL.

[78] M. Weiler, M. Althammer, M. Schreier, J. Lotze, M. Pernpeintner, S. Meyer, H. Huebl, R. Gross, A. Kamra, J. Xiao, Y. T. Chen, H. Jiao, G. E. Bauer & S. T. Goennenwein. Experimental test of the spin mixing interface conductivity concept. *Physical Review Letters* **111**, 176601 (2013), 1306.5012. URL.

[79] A. Brataas, Y. U. Nazarov & G. E. Bauer. Finite-element theory of transport in ferromagnet-normal metal systems. *Physical Review Letters* **84**, 2481–2484 (2000), 9906065. URL.

[80] M. Johnson & R. H. Silsbee. Coupling of electronic charge and spin at a ferromagnetic-paramagnetic metal interface. *Physical Review B* **37**, 5312–5325 (1988). URL.

[81] S. Sakurai, A. Namai, K. Hashimoto & S. I. Ohkoshi. First observation of phase transformation of all four Fe2O 3 phases ($\gamma \rightarrow \epsilon \rightarrow \beta \rightarrow \alpha$-phase). *Journal of the American Chemical Society* **131**, 18299–18303 (2009). URL.

[82] S. Sakurai, S. Kuroki, H. Tokoro, K. Hashimoto & S. I. Ohkoshi. Synthesis, crystal structure, and magnetic properties of ϵ-In xFe2-xO3 nanorod-shaped magnets. *Advanced Functional Materials* **17**, 2278–2282 (2007). URL.

[83] T. Danno, D. Nakatsuka, Y. Kusano, H. Asaoka, M. Nakanishi, T. Fujii, Y. Ikeda & J. Takada. Crystal structure of β-Fe2O3 and topotactic phase transformation to α-Fe2O3. *Crystal Growth and Design* **13**, 770–774 (2013). URL.

[84] H. M. Lu & X. K. Meng. Morin temperature and Néel temperature of hematite nanocrystals. *Journal of Physical Chemistry C* **114**, 21291–21295 (2010). URL.

[85] J. F. Garching. Spin Hall magnetoresistance in antiferromagnetic NiO and α-Fe 2 O 3. Tech. Rep. (2017).

[86] S. Alraddadi. The Electronic and Magnetic Properties of Ultrathin γ-Fe2O3 Films. In *IOP Conference Series: Materials Science and Engineering* Vol. 842012012 (Institute of Physics Publishing, 2020).

[87] R. A. Houze. Atmospheric dynamics. In *International Geophysics* Vol. 10425–46 (Academic Press, 2014).

[88] R. M. Cornell & U. Schwertmann. *The Iron Oxides* (Wiley, 2003).

[89] X. L. Huang, Y. Yang & J. Ding. Epitaxial growth of γ-Fe2O3 thin films on MgO substrates by pulsed laser deposition and their properties. *Acta Materialia* **61**, 548–557 (2013).

[90] X. Liu, C. F. Chang, A. D. Rata, A. C. Komarek & L. H. Tjeng. Fe3O4 thin films: Controlling and manipulating an elusive quantum material. *npj Quantum Materials* **1**, 1 (2016), 1610.02450. URL.

[91] Y. Peng, C. Park & D. E. Laughiin. Fe3O4 thin films sputter deposited from iron oxide targets. In *Journal of Applied Physics* Vol. 937957–7959 (American Institute of PhysicsAIP, 2003).

[92] X. Wang, Y. Liao, D. Zhang, T. Wen & Z. Zhong. A review of Fe3O4 thin films: Synthesis, modification and applications. *Journal of Materials Science and Technology* **34**, 1259–1272 (2018).

[93] J. X. Yin, Z. G. Liu, S. F. Wu, W. H. Wang, W. D. Kong, P. Richard, L. Yan & H. Ding. Unconventional magnetization of Fe3O4 thin film grown on amorphous SiO2 substrate. *AIP Advances* **6** (2016).

[94] W. Weiss & W. Ranke. Surface chemistry and catalysis on well-defined epitaxial iron-oxide layers (2002).

[95] L. Martín-García, I. Bernal-Villamil, M. Oujja, E. Carrasco, R. Gargallo-Caballero, M. Castillejo, J. F. Marco, S. Gallego & J. De La Figuera. Unconventional properties of nanometric FeO(111) films on Ru(0001): Stoichiometry and surface structure. *Journal of Materials Chemistry C* **4**, 1850–1859 (2016). URL.

[96] G. J. Abreu, R. Paniago & H. D. Pfannes. Growth of ultra-thin FeO(100) films on Ag(100): A combined XPS, LEED and CEMS study. *Journal of Magnetism and Magnetic Materials* **349**, 235–239 (2014).

[97] J. Gurgul, E. Młyńczak, N. Spiridis & J. Korecki. Layer-by-layer epitaxial growth of polar FeO(111) thin films on MgO(111). *Surface Science* **606**, 711–714 (2012).

[98] M. Opel. Spintronic oxides grown by laser-MBE. *Journal of Physics D: Applied Physics* **45** (2011), 1112.0751. URL.

[99] S. Geprägs. Magnetoelectric Interactions in Multiferroic Thin Films and Composites. Tech. Rep.

[100] K. I. Uchida, H. Adachi, T. Ota, H. Nakayama, S. Maekawa & E. Saitoh. Observation of longitudinal spin-Seebeck effect in magnetic insulators. *Applied Physics Letters* **97**, 103913 (2010). URL.

[101] M. Weiler, M. Althammer, F. D. Czeschka, H. Huebl, M. S. Wagner, M. Opel, I. M. Imort, G. Reiss, A. Thomas, R. Gross & S. T. Goennenwein. Local charge and spin currents in magnetothermal landscapes. *Physical Review Letters* **108**, 106602 (2012). URL.

[102] M. Schreier, N. Roschewsky, E. Dobler, S. Meyer, H. Huebl, R. Gross & S. T. Goennenwein. Current heating induced spin Seebeck effect. *Applied Physics Letters* **103**, 242404 (2013), 1309.6901. URL.

[103] K. M. Ganzhorn. Spin Transport in Insulating Ferrimagnets. Tech. Rep.

[104] W. Ranke, M. Ritter & W. Weiss. Crystal structures and growth mechanism for ultrathin films of ionic compound materials: FeO(111) on Pt(111). *Physical Review B - Condensed Matter and Materials Physics* **60**, 1527–1530 (1999). URL.

[105] L. Martín-García, I. Bernal-Villamil, M. Oujja, E. Carrasco, R. Gargallo-Caballero, M. Castillejo, J. F. Marco, S. Gallego & J. De La Figuera. Unconventional properties of

nanometric FeO(111) films on Ru(0001): Stoichiometry and surface structure. *Journal of Materials Chemistry C* **4**, 1850–1859 (2016). URL.

[106] J. W. Arblaster. Crystallographic Properties of Platinum | Johnson Matthey Technology Review (1997).

[107] J. M. Coey. *Magnetism and magnetic materials*, Vol. 9780521816 (Cambridge University Press, 2010).

[108] D. C. Giancoli. Physics : principles with applications (Book, 1995) [WorldCat.org] (1995).

[109] P. Ripka. Magnetic Sensors: Principles and Applications. In *Encyclopedia of Materials: Science and Technology* 1–11 (Elsevier, 2007).

[110] H. Ebert, A. Vernes & J. Banhart. Magnetoresistance, Anisotropic. In *Encyclopedia of Materials: Science and Technology* 5079–5083 (Elsevier, 2001).

Acknowledgements

At the end of this work, I want to thank all the people who supported me during this thesis and made this work possible. These are in particular:

- Prof. Dr. Rudolf Gross for accepting me as an exchange master student under DAAD 'KOSPIE' scholarship at the Chair of Technical Physics (E23) at TUM and giving me the opportunity to work on my master's thesis at the Walther-Meißner-Institut. I am also very grateful for your continuous support in the extension of my stay here at WMI, without that it would have not been possible to do this project.

- Prof. Dr. M.S. Ramachandra Rao for accepting and continuously guiding me during my exchange at WMI. Your courses made me very curious about nanotechnology and science in general. Also, for guiding and supporting me for my extension and later for my PhD application. I still remember your words, finally you have arrived at the right place, indeed it was.

- Dr. Matthias Opel for guiding me through everything. Starting with very patient and elaborate advice in the lab, that allowed me to understand different aspects of my work from measurement to interpretation of results. I am highly thankful to you for taking care of nearly everything for the extension of my stay. For helping me at every step in finding the PhD position. I am very grateful for the personal support that you have given, with your presence I never felt that I am so far away from home. During this experience of working with you I learned a lot on the professional level but more importantly on a personal level you showed me the path towards being a better human.

- Dr. Matthias Althammer for always motivating and inspiring me during the short conversations that we had in the corridors. Your valuable comments during DC meetings determined the interpretation of the results obtained within this work. I am grateful for your guidance and support in finding the PhD position.

- Dr. Stephan Geprägs for always taking care of all the trouble that I created, with a smile. Your comments in the DC meetings were highly valuable and helped a lot in the optimisation of the film growth.

- Manuel Müller for helping me with almost everything and answering my endless queries related to experiments, softwares or PhD application and of course for the late night words of wisdom.

- All the PhD students for their willingness to help me out, regardless of the kind of issue.

- Monika Scheufele and Philipp Schwenke for always helping me with the equipments and answering my endless queries and even staying few extra hours to help me with my work.

- All my Master colleagues, especially my office-mates Leonhard Hölscher, Niklas Bruckmoser, Ramona Stumberger for always cheering me and for creating a joyful environment in the office.
- The entire staff of the WMI especially secretary Emel Dönertas for always guiding me through different situations and for accepting me as a WMI member.
- My friends, namely Shishram, Satvik, Naman and Rehan for inspiring and being there whenever I needed them.
- My love Deepika, for absorbing my stress and frustration, for always giving me positivity and hope, this moon glows bright with you.
- My uncle Naresh for planting the seed of science during my childhood and always doing everything possible to make my life easier.
- My mother Shyamlata and my father Shersingh, for their unconditional love and support, for countless sacrifices you did for me. You made me the person I am today and all my achievements are only an embodiment and a consequence of your upbringing.
- For financial support, I am very grateful to DAAD (Deutscher Akademischer Austauschdienst) and WMI for giving me enough and more finances to have a comfortable stay in München and later in Garching.